PARTON DENSITIES FROM DEEP INELASTIC SCATTERING TO HADRONIC PROCESSES AT SUPER COLLIDER ENERGIES

M. Diemoz, F. Ferroni, E. Longo

Dipartimento di Fisica, Università "La Sapienza" di Roma
Istituto Nazionali di Fisica Nucleare, Sezione di Roma, Italy

and

G. Martinelli

CERN - Geneva

ABSTRACT

We give several sets of parton densities derived from recent measurements of structure functions in deep inelastic scattering. The difference among these densities reflects the uncertainties from deep inelastic data of different experiments, allowing an estimate of the error band for the predictions one may obtain for any given hadronic process at higher energy. The densities are available at any scale $Q^2 \leqslant 5 \cdot 10^9$ GeV^2 and $x \geqslant 5 \cdot 10^{-5}$ and include next-to-leading corrections as well as threshold effects due to heavy flavours. A comparison with a large set of data in a wide range of scales (Drell-Yan, W and Z production, etc.) is also presented.

CERN-TH.4751/87
June 1987

1. Introduction

High statistics experiments on deep inelastic scattering have been performed in the last decade. As a consequence detailed information on the structure functions is now available. This information can be used to derive quark and gluon densities in the framework of the QCD improved parton model with a good degree of accuracy. These densities are the fundamental ingredients to make quantitative predictions for hadronic processes at very high energies.

In this paper we present new sets of parton parametrizations by analyzing recent experimental results on deep inelastic scattering. Our study differs with respect to previous works on the same subject [1, 2, 3] in many respects:

1) Valence quark, antiquark and gluon densities have been extracted from the data at the reference scale $Q_0^2 = 10$ GeV^2 taking consistently into account all the next to leading corrections at order α_s.

2) Several sets of parton parametrizations, obtained by comparing different experimental determinations of the structure functions, are presented. Among them we indicate our preferred one, called "average" in the following. However by using the different sets presented below it is possible to give, for any hadronic process, an estimate of the error which stems from the original uncertainties in the measurement of the structure functions. We show in sect.5 that many experimental results coming from processes different from deep inelastic scattering lie within the band of error determined by using our different sets of parton densities. Thus we are confident that our theoretical predictions at much higher and still unexplored energies (HERA and Super Colliders) will constitute a reliable reference, within the band of error, for the experimental results still to come.

3) The parton densities are evolved up to and including next-to-leading corrections and heavy quark thresholds; these latter according to the recent theoretical analysis of ref. [4] .

4) We do provide a computer program to evolve the parton densities at any scale

$Q^2 \leq 5 \cdot 10^9$ GeV^2 and $x \geq 5 \cdot 10^{-5}$. In this program it is possible to vary not only the form of the input parton densities but also the definition (necessary beyond the leading logarithms) of the parton densities themselves, which in our standard version is the one suggested in refs. [5,6].

The paper is organized as follows: in sect.2 we recall the essential notation and formulae for deep inelastic scattering in the framework of the parton model; in sect.3 the evolution of the parton densities beyond the leading log approximation is discussed and all the relevant formulae given; in sect.4 the determination of the parton densities and of Λ_{QCD} from the structure functions is presented; in sect.5 we compare the predictions obtained by using our parametrizations with different experimental measurements in a wide range of energies. Finally in sect.6 we discuss the consequences of the input uncertainties when evolving the parton densities to scales appropriate for Super Collider physics. A brief explanation of the available FORTRAN code for the calculation of the evolution of the parton densities is finally provided in the Appendix.

2. Definition of the parton densities

In this section we specify the notation and give the definition of our parton densities beyond the leading logarithmic approximation.

Let us introduce the well-known structure functions of deep inelastic scattering $F_i(x, Q^2)$ $(i = 1,2,3)$, as they enter in the neutrino and antineutrino cross sections. Q^2 indicates the absolute value of q^2, where q is the momentum carried by the current, and $x = Q^2/2P \cdot q$, where P is the nucleon momentum

$$\frac{d^2\sigma^{\nu,\bar{\nu}}}{dx dy} = \frac{G^2 s}{2\pi} \left(xy^2 F_1^{\nu,\bar{\nu}} + \left(1 - y - \frac{Mxy}{2E}\right) F_2^{\nu,\bar{\nu}} \pm \left(y - \frac{y^2}{2}\right) xF_3^{\nu,\bar{\nu}} \right) \tag{2.1}$$

where $y = P \cdot q/P \cdot k$ and k indicates the lepton momentum.

The structure functions can be written in the framework of the QCD improved parton model as suitable convolutions of quark, antiquark and gluon densities. At the leading logarithmic approximation (LLA) the results of the QCD corrections can be interpreted by saying that the $F_i(x,Q^2)$ are given by the naive parton model formulae expressed in terms of Q^2 dependent effective parton densities obeying to the first order Altarelli-Parisi evolution equations.

Beyond the LLA the expressions of the $F_i(x,Q^2)$ deviate from the parton model formulae by terms of order α_s (coefficient functions) and the evolution equations for the parton densities must include the next to leading terms of the anomalous dimensions. The explicit form of the corrections to structure functions depends on the definition of the effective parton densities beyond the LLA. Different definitions of the parton densities will give of course the same physical results.

We chose our definition of quark densities by demanding that $F_2(x,Q^2)$ have to maintain the same form as in the naive parton model [5,6]. More explicitly:

$$\begin{aligned} F_2(x,Q^2) = x\int_x^1 \frac{dy}{y}(q_f(y,Q^2)+\overline{q}_f(y,Q^2))\left(\delta(1-\frac{x}{y})+\frac{\alpha_s(Q^2)}{2\pi}C^2_{qq}(\frac{x}{y})\right)+ \\ +\frac{\alpha_s(Q^2)}{2\pi}2G(y,Q^2)C^2_{qG}(\frac{x}{y}) \rightarrow x[q_f(x,Q^2)+\overline{q}_f(x,Q^2)] \end{aligned} \tag{2.2}$$

C^2_{qq} and C^2_{qG} are the coefficient functions for F_2 and eq.(2.2) refers to one flavour, V-A coupling. This choice guarantees that the quark densities obey the conservation of charge because of the Adler sum rule, which is valid to all orders in perturbation theory:

$$\int_0^1 dx[q_f(x,Q^2)-\overline{q}_f(x,Q^2)] = v_f \tag{2.3}$$

where v_f is the valence value for a given flavour.

We introduce the notation:

$$\Sigma(x,Q^2) = \sum_f [q_f(x,Q^2)+\overline{q}_f(x,Q^2)]$$

and with the definition of eq.(2.2) we find:

$$\begin{aligned} 2F_1(x,Q^2) &= \int_x^1 \frac{dy}{y}(\Sigma(y,Q^2)\left(\delta(1-\frac{x}{y})-\frac{\alpha_s(Q^2)}{2\pi}C^L_{qq}(\frac{x}{y})\right) \\ &\quad -2N_f G(y,Q^2)\frac{\alpha_s(Q^2)}{2\pi}C^L_{qG}(\frac{x}{y})) \\ F_3(x,Q^2) &= \int_x^1 \frac{dy}{y}\sum_f(q_f(y,Q^2)-\overline{q}_f(y,Q^2))\left(\delta(1-\frac{x}{y})-\frac{\alpha_s(Q^2)}{2\pi}\tilde{C}^3_{qq}(\frac{x}{y})\right)= \\ &= F^0_3(x,Q^2)-\Delta F_3(x,Q^2) \end{aligned} \tag{2.4}$$

where the coefficient functions $C^i_{pp'}$, computed in refs. [5,6], are:

$$\begin{aligned} C^L_{qq}(z) &= 8z/3 \\ C^L_{qG}(z) &= 2z(1-z) \\ \tilde{C}^3_{qq}(z) &= C^3_{qq} - C^2_{qq} = 4(1+z)/3 \quad . \end{aligned} \tag{2.5}$$

From eqs.(2.2) and (2.4) one gets:

$$\begin{aligned} F_L(x,Q^2) &= F_2(x,Q^2) - 2xF_1(x,Q^2) = \\ &= \frac{\alpha_s(Q^2)}{2\pi} x \int_x^1 \frac{dy}{y} \left(\Sigma(x,Q^2) C^L_{qq}(\frac{x}{y}) + 2N_f G(y,Q^2) C^L_{qG}(\frac{x}{y}) \right) \end{aligned} \tag{2.6}$$

and the modified Gross-Llewellyn Smith relation becomes

$$\int_0^1 dx F_3 = (1 - \frac{\alpha_s}{\pi}) \sum_f v_f \quad . \tag{2.7}$$

We fix the gluon density beyond the LLA by demanding momentum conservation:

$$\int_0^1 dx x [\sum_f (q_f(x,Q^2) + \bar{q}_f(x,Q^2)) + G(x,Q^2)] = 1 \tag{2.8}$$

To this purpose we redefine the gluon density as follows*:

$$\begin{aligned} G(x,Q^2) \rightarrow & G(x,Q^2) - \frac{\alpha_s(Q^2)}{2\pi} \\ & \int_x^1 \frac{dy}{y} \left(\Sigma(y,Q^2) C^2_{qq}(\frac{x}{y}) + 2N_f G(y,Q^2) C^2_{qG}(\frac{x}{y}) \right) + O(\alpha_s^2) \end{aligned} \tag{2.9}$$

Note that at first order the expressions of $F_i(x,Q^2)$ are not affected by the choice of $G(x,Q^2)$ since the gluons first appear at order α_s in deep inelastic scattering.

---

* A different and more appropriate definition of the gluon density can be found by considering the next to leading corrections to some strong interaction hard process where gluons interact at the lowest non trivial order in α_s such as, for example, the two jet cross section in proton-proton and proton-antiproton collisions. These corrections have not been computed so far.

3. Evolution of the parton densities

The evolution equations for the quark, antiquark and gluon densities can be written as:

$$\frac{dq_i}{d(lnQ^2)} = \frac{\alpha_s}{2\pi}\left(\sum_j (P_{q_iq_j}\otimes q_j + P_{q_i\bar{q}_j}\otimes \bar{q}_j) + P_{q_iG}\otimes G\right)$$

$$\frac{d\bar{q}_i}{d(lnQ^2)} = \frac{\alpha_s}{2\pi}\left(\sum_j (P_{\bar{q}_iq_j}\otimes q_j + P_{\bar{q}_i\bar{q}_j}\otimes \bar{q}_j) + P_{\bar{q}_iG}\otimes G\right) \qquad (3.1)$$

$$\frac{dG}{d(lnQ^2)} = \frac{\alpha_s}{2\pi}\left(\sum_j (P_{Gq_j}\otimes q_j + P_{G\bar{q}_j}\otimes \bar{q}_j) + P_{GG}\otimes G\right)$$

where $P \otimes f$ denotes:

$$P\otimes f(x) = \int_x^1 \frac{dz}{z}P(z)f(\frac{x}{z})$$

The solution of equations (3.1), together with the renormalization group equation for the running coupling constant,

$$\frac{d\alpha_s}{d(lnQ^2)} = -\frac{\beta_0}{4\pi}\alpha_s^2 - \frac{\beta_1}{16\pi^2}\alpha_s^3 \qquad (3.2)$$

where

$$\beta_0 = 11 - \frac{2}{3}N_f$$

$$\beta_1 = 102 - \frac{38}{3}N_f \quad ,$$

allows the computation of the parton densities at any scale Q^2 once the initial conditions are known.

In the following, all results at NL order are derived assuming $\Lambda_{\overline{MS}} = 300$ MeV; whereas for the evolution at leading order we used $\Lambda_{LO} = 200$ MeV (for a review of recent results see [7]).

A more convenient way of writing eqs. (3.1) is the following. We introduce the quantities:

$$V_i(x,Q^2) = q_i(x,Q^2) - \bar{q}_i(x,Q^2) \qquad (3.3)$$

and given $q_i^+ = q_i + \bar{q}_i$, we define:

$$
\begin{aligned}
&T_8(x,Q^2) = u^+(x,Q^2) + d^+(x,Q^2) - 2s^+(x,Q^2)\\
&T_{15}(x,Q^2) = u^+(x,Q^2) + d^+(x,Q^2) + s^+(x,Q^2) - 3c^+(x,Q^2)\\
&T_{24}(x,Q^2) = u^+(x,Q^2) + d^+(x,Q^2) + s^+(x,Q^2) + c^+(x,Q^2) - 4b^+(x,Q^2)\\
&T_{35}(x,Q^2) = u^+(x,Q^2) + d^+(x,Q^2) + s^+(x,Q^2) + c^+(x,Q^2) + b^+(x,Q^2) - 5t^+(x,Q^2)
\end{aligned}
$$

u, d, s, c, b, t, are respectively the up, down, strange, charm, bottom and top densities. Defining

$$
\begin{aligned}
P_{q_iq_j} &= \delta_{ij}P^V_{qq} + P^S_{qq}\\
P_{q_i\bar{q}_j} &= \delta_{ij}P^V_{q\bar{q}} + P^S_{q\bar{q}}
\end{aligned}
$$

and using the following relations (valid at the next to leading order):

$$
\begin{aligned}
&P^S_{qq} = P^S_{q\bar{q}}\\
&P_{q_iq_j} = P_{\bar{q}_i\bar{q}_j}; \qquad P_{q_i\bar{q}_j} = P_{\bar{q}_iq_j}\\
&P_{q_iG} = P_{\bar{q}_iG} \equiv P_{qG}; \qquad P_{Gq_i} = P_{G\bar{q}_i} \equiv P_{Gq}.
\end{aligned}
\tag{3.4}
$$

eqs. (3.1) become:

$$
\begin{aligned}
\frac{dV_i(x,Q^2)}{d(lnQ^2)} &= \frac{\alpha_s}{2\pi}[P_- \otimes V_i(x,Q^2)]\\
\frac{dT_i(x,Q^2)}{d(lnQ^2)} &= \frac{\alpha_s}{2\pi}[P_+ \otimes T_i(x,Q^2)]\\
\frac{d}{d(lnQ^2)}\begin{pmatrix}\Sigma(x,Q^2)\\ G(x,Q^2)\end{pmatrix} &= \frac{\alpha_s}{2\pi}\begin{pmatrix}P_{FF} & P_{FG}\\ P_{GF} & P_{GG}\end{pmatrix} \otimes \begin{pmatrix}\Sigma(x,Q^2)\\ G(x,Q^2)\end{pmatrix} \equiv \frac{\alpha_s}{2\pi}\hat{P} \otimes \begin{pmatrix}\Sigma(x,Q^2)\\ G(x,Q^2)\end{pmatrix}
\end{aligned}
\tag{3.5}
$$

where:

$$
\begin{aligned}
P_\pm &= P^V_{qq} \pm P^V_{q\bar{q}}\\
P_{FF} &= P_+ + 2N_fP^S_{qq}\\
P_{FG} &= 2N_fP_{qG}\\
P_{GF} &= P_{Gq} \quad .
\end{aligned}
$$

We assume that at our reference scale Q_0^2 the charm threshold is already open, namely $N_f = 4$, but $c(x,Q_0^2) \sim 0$. The non singlet parton densities T_{24} and T_{35} will evolve like the singlet density Σ below the threshold for producing the b or t quarks respectively. The T_i will be used to evaluate the c, b, and t quark densities separately.

Following reference [8] we change the evolution variable $\ln(Q^2)$ into:

$$t = \frac{2}{\beta_0} ln \left(\frac{\alpha_s(Q_0^2)}{\alpha_s(Q^2)} \right) \tag{3.6}$$

and we expand the Altarelli-Parisi kernels P in powers of α_s:

$$P = P^{(o)} + \frac{\alpha_s}{2\pi} P^{(1)} \quad .$$

Eqs. (3.5) then become:

$$\begin{aligned}
\frac{dV_i(x,t)}{dt} &= [P^{(o)} + \frac{\alpha_s}{2\pi}(P_-^{(1)} - \frac{\beta_1}{2\beta_0}P^{(o)})] \otimes V_i(x,t) \\
&\equiv (P^{(o)} + \frac{\alpha_s}{2\pi}R_-) \otimes V_i(x,t) \\
\frac{dT_i(x,t)}{dt} &= [P^{(o)} + \frac{\alpha_s}{2\pi}(P_+^{(1)} - \frac{\beta_1}{2\beta_0}P^{(o)})] \otimes T_i(x,t) \\
&\equiv (P^{(o)} + \frac{\alpha_s}{2\pi}R_+) \otimes T_i(x,t) \\
\frac{d}{dt}\begin{pmatrix} \Sigma(x,t) \\ G(x,t) \end{pmatrix} &= [\hat{P}^{(o)} + \frac{\alpha_s}{2\pi}(\hat{P}^{(1)} - \frac{\beta_1}{2\beta_0}\hat{P}^{(o)})] \otimes \begin{pmatrix} \Sigma(x,t) \\ G(x,t) \end{pmatrix} \\
&\equiv (\hat{P}^{(o)} + \frac{\alpha_s}{2\pi}\hat{R}) \otimes \begin{pmatrix} \Sigma(x,t) \\ G(x,t) \end{pmatrix}
\end{aligned} \tag{3.7}$$

where we have used $P^{(o)} = P_+^{(o)} = P_-^{(o)}$.

Finally we have to modify the second order Altarelli-Parisi kernels $P^{(1)}$ to include into the definition of the parton densities the coefficient functions (as indicated in sec. 2). Writing the matrix of the coefficient functions as:

$$\hat{C} = \hat{C}^{(o)} + \frac{\alpha_s}{2\pi}\hat{C}^{(1)}$$

then:

$$\begin{aligned}
&P_\pm^{(1)} \to P_\pm^{(1)} - \frac{\beta_0}{2}C_{qq}^{(1)} \\
&\hat{P}^{(1)} \to \hat{P}^{(1)} + [\hat{C}^{(1)}, \hat{P}^{(o)}] - \frac{\beta_0}{2}\hat{C}^{(1)} \quad .
\end{aligned} \tag{3.8}$$

In our case we simply redefine the quark and antiquark densities incorporating the next to leading corrections to F_2 in q, $\overline{q}$ and imposing the total momentum conservation. Then:

$$\hat{C}^{(1)} = \begin{pmatrix} C_{qq}^2 & C_{qG}^2 \\ -C_{qq}^2 & -2N_f C_{qG}^2 \end{pmatrix} \tag{3.9}$$

It is a trivial change to define the parton densities with a different set of coefficient functions. In particular we stress again the importance of using in the future a definition of the gluon taken from some strong interaction process such as the two jet cross section in hadron-hadron collisions.

Several methods to evolve the parton densities were used in the literature. We find very convenient to Mellin transform the parton densities and to solve the equations in Mellin space. This method was already used, at the leading logarithmic approximation in ref. [9]. The advantage with respect to the alternative method of evolving the densities by discretizing the evolution time t in eqs. (3.7) is that accumulation of the rounding errors, when evolving at very large scales, is avoided. A drawback (however minor) is that an analytic expression of the parton densities at the reference scale Q_0^2 must be provided (see section 4).

We define the following Mellin transforms:

$$\begin{aligned} f(n) &= \int_0^1 dx x^{n-1} f(x) \\ f(x) &= \frac{1}{2\pi i}\int_{-i\infty}^{+i\infty} dn x^{-n} f(n) \quad . \end{aligned} \tag{3.10}$$

In Mellin space the convolution $P \otimes f$ reduces to a product:

$$P \otimes f(x) = \int_x^1 \frac{dz}{z} P(z) f(\frac{x}{z}) \quad \rightarrow \quad P(n) f(n) \equiv P f(n) \quad .$$

Eqs. 3.7 become[*]

$$\begin{aligned} \frac{dV_i(n,t)}{dt} &= [P^{(o)}(n) + \frac{\alpha_s}{2\pi} R_-(n)] V_i(n,t) \\ \frac{dT_i(n,t)}{dt} &= [P^{(o)}(n) + \frac{\alpha_s}{2\pi} R_+(n)] T_i(n,t) \\ \frac{d}{dt}\begin{pmatrix} \Sigma(n,t) \\ G(n,t) \end{pmatrix} &= [\hat{P}^{(o)}(n) + \frac{\alpha_s}{2\pi}\hat{R}(n)] \begin{pmatrix} \Sigma(n,t) \\ G(n,t) \end{pmatrix} \quad . \end{aligned} \tag{3.11}$$

The solution for the non-singlets $V_i(n.t)$ and $T_i(n,t)$ is immediately found:

$$V_i(n,t) = (1 + \frac{\alpha_s(t) - \alpha_s(0)}{2\pi} R_-) e^{P^{(o)} t} \quad V_i(n,0) \tag{3.12}$$

---

[*] $P_\pm(n)$ are related to even (odd) momenta of the anomalous dimensions computed in the framework of the operator product expansion

$$T_i(n,t) = (1 + \frac{\alpha_s(t) - \alpha_s(0)}{2\pi} R_+) e^{P^{(o)}t} \quad T_i(n,0) \tag{3.13}$$

We have imposed initial conditions different from those of ref. [8], namely without any extra term of order $\alpha_s(0)$ at the reference scale.

The solution of the evolution equations for the sea and gluon densities is somehow more complicated. Given the eigenvalues of the matrix $\hat{P}$:

$$\lambda_\pm = \frac{1}{2}(P^{(o)}_{FF}(n) + P^{(o)}_{GG}(n) \pm \sqrt{(P^{(o)}_{FF}(n) - P^{(o)}_{GG}(n))^2 + 4P^{(o)}_{FG}(n)P^{(o)}_{GF}(n)})$$

we define two projection matrices:

$$M_+ = \frac{\hat{P}^{(o)}(n) - \lambda_- 1}{\lambda_+ - \lambda_-} \qquad M_- = \frac{-\hat{P}^{(o)}(n) + \lambda_+ 1}{\lambda_+ - \lambda_-}$$

where 1 is the 2x2 unity matrix. The projectors $M_\pm$ have the following properties:

$$M_+^2 = M_+ \quad M_-^2 = M_- \quad M_+M_- = M_-M_+ = 0 \quad M_+ + M_- = 1 \quad .$$

The solution for Σ and G is then:

$$\begin{aligned} \begin{pmatrix} \Sigma(n,t) \\ G(n,t) \end{pmatrix} &= [(M_+ + \frac{\alpha_s(t)}{2\pi}\rho_+ - \frac{\alpha_s(0)}{2\pi} M_+(\rho_+ + \rho_-))e^{\lambda_+ t} \quad + \\ + \quad & (M_- + \frac{\alpha_s(t)}{2\pi}\rho_- - \frac{\alpha_s(0)}{2\pi} M_-(\rho_+ + \rho_-))e^{\lambda_- t}] \begin{pmatrix} \Sigma(n,0) \\ G(n,0) \end{pmatrix} \quad . \end{aligned} \tag{3.14}$$

In eq. (3.14) terms of order $\alpha_s(t)\alpha_s(0)$ have been eliminated. The matrices ρ_+ e ρ_- are defined as:

$$\rho_+ = -\frac{2}{\beta_0} M_+ \hat{R} M_+ + \frac{M_- \hat{R} M_+}{\lambda_+ - \lambda_- - \beta_0/2}$$

$$\rho_- = -\frac{2}{\beta_0} M_- \hat{R} M_- + \frac{M_+ \hat{R} M_-}{\lambda_- - \lambda_+ - \beta_0/2}$$

From eqs. (3.14) it is easy to verify that $\Sigma(n, t=0) = \Sigma(n,0)$ and $G(n,t=0) = G(n,0)$.

The β function, the anomalous dimensions and the coefficient functions depend on N_f. For this reason a further complication arises when the bottom and top flavours are activated. Short of a complete treatement of threshold effects, we have changed all the N_f dependent quantities when crossing a conventional threshold taken to be $Q_f^2 = m_f^2$. For $Q^2 \gg Q_{b,t}^2$ we have verified that our results for the b and t densities are not too sensitive to the precise value we have used for $m_{b,t}$ ($m_b = 4.5$ GeV, $m_t = 40$ GeV) when varying $m_{b,t}$ in a reasonably small range around their central values (e. g. $4 \leq m_b \leq 5$ GeV).

We conclude this section with two technical details. The evolution of the Mellin transforms of the parton densities needs only multiplication by suitable complex matrices and factors as it can be seen from eqs. (3.12), (3.13) and (3.14). However, to obtain the densities in x we have to perform numerically the inverse Mellin transform of these equations. In practice we performed the integral:

$$f(x) = \frac{1}{2\pi i}\left(\int_{\Re-i\Im}^{\Re_0} f(n)x^{-n}dn + \int_{\Re_0}^{\Re+i\Im} f(n)x^{-n}dn\right) \quad .$$

$\Re_0$, $\Re$ and $\Im$ were chosen in a different way for non-singlet and singlet densities and for $x \leq 0.5$ or $x \geq 0.5$ in order to maximize stability and precision of the results. The values of $\Re_0$, $\Re$ and $\Im$ are reported in tab. 3.1.

Finally we have used for the anomalous dimensions and the coefficient functions the results of [10].

4. Input parton densities

4.1 Data sets.

Deep inelastic muon and neutrino experiments [11 – 17] are the main source of high statistics data samples. In principle, both classes of experiments represent a powerful tool to determine, within the frame of the QCD improved parton model, the parameter Λ_{QCD}, the gluon density and the flavour content of the nucleons. However, although muon experiments measure F_2 in a very precise way, they cannot determine xF_3 which is a unique feature of parity violating weak interaction. Therefore we have used the results coming from the neutrino experiments BEBC [14], CCFRR [15], CDHS [16] and CHARM [17] as input for QCD evolution of the gluon, the valence and the sea densities. Nevertheless we do not discard the information coming from muon experiments, paying attention to the possible influence of the so called "EMC effect", by monitoring our input densities on the available muon data as well as on precise data coming from other processes

(Drell-Yan) [18 – 20] in a region not far from our input scale $Q_0^2 = 10$ GeV^2 (see sect. 5).

4.2 The valence distribution

To determine the valence quark distributions xu_v and xd_v we have combined the results obtained for xF_3 from the experiments BEBC [14], CCFRR [15], CDHS [16] and CHARM [17] at the scale Q_0^2.

To separate the u_v and the d_v contributions to xF_3 we assume to be valid the relation

$$\frac{d_v}{u_v} = r(1-x). \tag{4.1}$$

This choice is well founded because of the measurement ratio published by BEBC [21] and CDHS [22]. Moreover recent results by BEBC [14] indicate that the relation in eq. (4.1) is to a large extent scale independent in the Q^2 range $1 - 100$ GeV^2.

With our definition of the parton densities at the next to leading approximation (see section 2) the experimentally determined xF_3 and the valence quark densities are in the relation:

$$\begin{aligned} xF_3^{exp}(x,Q^2) &= xu_v(x,Q^2) + xd_v(x,Q^2) - \\ &- \frac{2}{3}\frac{\alpha_s(Q^2)}{\pi} x \int_x^1 \frac{dz}{z}[u_v(z,Q^2) + d_v(z,Q^2)](1+\frac{x}{z}) \end{aligned} \tag{4.2}$$

We have then carried out a fit to xF_3 at Q_0^2 in order to extract a parametrization for xu_v imposing:

$$\begin{aligned} &\int_0^1 (u_v + d_v)dx = 3 \\ &\int_0^1 u_v dx = 2 \end{aligned} \tag{4.3}$$

so that the modified Gross-Llewellin Smith sum rule $\int_0^1 F_3 dx = 3(1 - \alpha_s/\pi)$ is automatically satisfied.

As a result for the combined average we obtain:

$$xu_v = 2.26x^{0.54}(1-x)^{2.52}[1 - 1.617(1-x) + 3.647(1-x)^2 - 1.998(1-x)^3] \tag{4.4}$$

and $r = 0.57$. The parameter r comes out to be approximatively fixed to this value by the form (4.1) assumed for the d_v/u_v ratio and by the behaviour $F_3 \sim (1-x)^3$ for $x \to 1$ [23].

Concerning the evaluation of the uncertainties on the valence distribution we notice that eqs. (4.3) impose a strong constraint, once an analytical form for u_v is fixed. This strongly reduces the possibility to vary the parameters of the distribution itself inside the statistical errors of the data.

We believe that the best evaluation of the experimental uncertainties on these densities is to assume the harder xF_3 (the higher in the high x region) represented by BEBC data and the softer xF_3 (the lower in the high x region) given by CHARM data, maintaining the normalization of F_3, as the two extreme possible cases representing the systematic uncertainty on the average distribution. The statistical error on the valence density is then neglected. The BEBC data come from a light target while the CHARM ones from a heavy target: our evaluation of the uncertainties somehow includes also possible nuclear effects as those observed by the EMC collaboration [24]. In fact what can be said without invoking any model is that in the region $x > 0.35$, where the contribution of the sea distribution is negligible and where the EMC, SLAC [25,26] and BCDMS [27] data agree, the valence measured inside a heavy target is softer than the one measured inside a light target.

Performing the fits to BEBC and CHARM data, under the conditions previously discussed, we obtain for the harder case:

$$xu_v = 0.237x^{0.38}(1-x)^{2.11}[1 + 17.724(1-x) - 9.993(1-x)^2 - 4.439(1-x)^3] \quad (4.5)$$

with $r = 0.574$, and for the softer one:

$$xu_v = 3.85x^{0.65}(1-x)^{2.89}[1 - 1.057(1-x) + 0.243(1-x)^2 + 0.897(1-x)^3] \quad (4.6)$$

with $r = 0.568$. xF_3 from the three valence distributions (hard, soft, average) are shown in fig. 4.1 together with the experimental data.

The effect of the $O(\alpha_s)$ corrections on the valence quark distribution $x(u_v + d_v)$ are tiny and they are shown in fig. 4.2.

4.3 The antiquark distribution

The measurements performed by neutrino experiments give through the combination of cross sections

$$\frac{2\pi}{G^2 s}\left(\frac{d^2\sigma^{\overline{\nu}}}{dxdy} - (1-y)^2\frac{d^2\sigma^{\nu}}{dxdy}\right)$$

the experimental antiquark distribution $\overline{q}^{\nu} = \overline{u} + \overline{d} + 2\overline{s}$.

The experimental results obtained for this quantity from CDHS [16] and CHARM [17] are in good agreement. A quite precise determination of the antiquark distribution can then be obtained by combining the existing data at different values of Q^2 in an appropriate QCD analysis and calculating via interpolation the values at $Q_0^2 = 10$ GeV^2.

To disentangle the flavour composition of the antiquark distribution we assumed $\overline{u} = \overline{d}$ [14] and from dimuon event analysis [28] we have fixed the strange quark density to be

$$\overline{s} = 0.2(\overline{u} + \overline{d}) = 0.4\overline{u} \quad .$$

The maximum variation of the percentage of s quarks was evaluated by the CDHS collaboration to be of the order of 20%.

Data on charmed sea [29] are still very poor. We have assumed that at $Q^2 = 10$ GeV^2 this density is negligible although the threshold for the production of c quarks is already crossed.

Finally the correction due to F_L as expected by QCD as well as the one due to F_3 have been included.

The experimentally determined distribution $\overline{q}^{\nu}$ is related to the NL defined antiquark distribution in the following way:

$$x\overline{q}(x,Q^2) = x\overline{q}^{\nu}(x,Q^2) + \frac{y^2}{2}F_L(x,Q^2) - \frac{1}{2}\Delta F_3(x,Q^2) \tag{4.7}$$

The two corrections are both of the order of 10% at $x \sim 0.01$ but cancel each other at the level of 1%.

We have fitted the overall corrected points obtaining the following distribution:

$$x\overline{q} = 0.70(1-x)^{8.5}(1 - 4.18x + 20.3x^2 - 15.3x^3) \tag{4.8}$$

The shape of $\bar{q}$ has been fixed by taking also into account the data for Drell-Yan processes in proton-nucleon collisions (cfr. sect. 5.2). Actually these processes are rather sensitive to $\bar{q}$, since they involve valence-sea annihilation. The uncertainty on the sea resulting from statistical and systematical experimental errors, from the uncertainty on the strange sea contribution and on the measurements of the neutrino and antineutrino total cross sections [30], owing to the circumstance that the sea is not on its own constrained by any sum rule, can be quantified as a possible variation of the normalization coefficient by +15%, −10%.

4.4 The gluon distribution

Contrary to quark densities, the gluon density is correlated, beside a particular set of data, to a specific QCD analysis. Probably due to this fact, the existing results obtained by the CDHS [16] and CHARM [17] collaborations are not in agreement especially in the low x region. For this reason we have not found worthwhile to combine the results on the determination of xG and we will consider them separately.

We have fitted the gluon as determined by CHARM directly to its Mellin transform $G(n) = \int_0^1 x^{n-1}G(x)dx$ choosing for $G(n)$ the following expression:

$$G(n, A, \alpha, \beta, \delta) = A\frac{\Gamma(\alpha+n-1)\Gamma(\beta+1)}{\Gamma(\alpha+\beta+n)}exp[-\delta ln(n)ln(ln(n))] \qquad (4.9)$$

and obtaining:

$$A = 1.46, \quad \alpha = -0.145, \quad \beta = 3.98, \quad \delta = 0.926$$

The term depending on δ in eq. (4.9) has been included trying to take into account the fact that $xG(x)$ behaves effectively like $(1-x)^{\delta'(x)}$, with δ' varying with x as $x \rightarrow 1$*.

The evaluation of the uncertainties on the gluon distribution at the input scale is very important. At $Q^2 = 10^6$ GeV^2, very far from Q_0^2, the amount of the gluon density coming solely from the evolution of the input valence at reasonable values of x is negligible with

---

* A good fit to the data is given in [31]

respect to the entity of the whole distribution and the echo of the input gluon is still the most relevant contribution.

The experimental uncertainties on the gluon distribution is expressed by the CHARM collaboration as a ($\pm 1\sigma$) confidence belt that contains also the one due to the error on the determination of the parameter Λ_{QCD}. Inside this belt we determined the softer and the harder distribution fixing the normalization to the central value 0.52 with a tolerance of $\pm 10\%$. For the parameters of the soft distribution we obtained

$$A = 1.37, \quad \alpha = -0.235, \quad \beta = 4.94, \quad \delta = 0.780$$

and for those relative to the hard distribution

$$A = 1.44, \quad \alpha = -0.126, \quad \beta = 3.55, \quad \delta = 0.860 \quad .$$

We have parametrized the gluon density determined by the CDHS collaboration[32] with the simple form:

$$xG(x, Q_0^2) = 3.34(1-x)^{5.06}(1-0.177x) \quad . \tag{4.10}$$

The curves for xG inside the CHARM confidence belt are shown in fig. 4.3 together with the parametrization derived from the CDHS data.

4.5 Comparison with other parametrizations at Q_0^2

In this subsection we compare our results for the parton densities at the reference scale Q_0^2 with the parametrizations given by Duke and Owens [2] (DO, set 1, $\Lambda_{LO} = 200$ MeV) and by Eichten, Hinchliffe, Lane and Quigg [3] (EHLQ, $\Lambda_{LO} = 200$ MeV).

In fig. 4.4 our valence distributions (average, harder and softer) are given together with those of DO and EHQL. The latter are contained in the error band but in the region $x \geq 0.7$ where the experimental data are scarce and the curves are determined only by the choice of the functional dependence of the parametrization on x.

Fig. 4.5 shows the distributions for the CHARM gluon density; DO and EHLQ make both use of different sets of data, all including the CDHS determination and this explains the difference, especially at low x.

In fig. 4.6 our antiquark density is given with its error band. The difference with the corresponding result from DO is possibly due to the fact that these authors apply a rescaling factor to data from different experiments.

5. Comparison with other experimental data

In this section the parton densities derived from the analysis of neutrino and antineutrino deep inelastic scattering will be used to predict other quantities of experimental interest and compared with existing results. In some cases we will also compare our results with those obtained by using other parametrizations (DO [2] and EHLQ [3]).

5.1 Electroproduction.

In fig. 5.1 the ratio $F_2^{\mu p}(x,Q^2)/(1-x^3)$ at $Q^2 = 20$ GeV^2 is shown. $F_2^{\mu p}$ has been measured by the EMC collaboration on a H_2 target [11]. Our prediction is represented by a solid curve, those by DO and EHLQ by a dashed and by a dotted curve respectively. At small x the difference in shape between our result and the experimental data originates from the different behaviour observed on light targets with respect to heavy targets by the EMC collaboration. This effect however has not been observed in electroproduction at SLAC [25,26] and it has not been confirmed by the more recent measurements by the BCDMS collaboration [27], nor by the latest EMC data [33]. The curve by DO shows a better agreement: in fact they normalized their parametrization precisely on these data. A better agreement is found if we use our "hard" valence parametrization, as shown in fig. 5.2. In fig. 5.3 the EMC measurement [12] for $F_2^{\mu N}$ on an iron target at $Q^2 = 22.5$ GeV^2 is given. In this case there is good agreement between the curve obtained with the "average" parametrization and the data. DO and EHLQ results deviate from the experimental points at large and small x respectively.

Fig. 5.4 shows the data from [34] and [35] and theoretical predictions for the ratio $F_2^{\mu n}/F_2^{\mu p}$ at $Q^2 = 10$ GeV^2. Given the difference between the measurements of the two groups, one can say that our curve is in reasonable agreement with the data. The dashed curve (DO) is systematically above the experimental points. The reason for this is that DO fixed the d_v/u_v ratio by fitting the low Q^2 data [25,26] (SLAC). These data can hardly be accommodated in a coherent way with the more recent results at highest Q^2 from muon deep inelastic scattering [35] (fig. 5.5). DO parametrizations badly fail in reproducing d_v/u_v as measured by BEBC [21] and CDHS [22] as shown in fig. 5.6. On the other hand it is not surprising that our curve fits nicely these data since we imposed $d_v/u_v \propto (1-x)^\delta$ with $\delta = 1$. To evaluate the sensitivity of the results to this condition we also varied δ between 1.2 and .8. No appreciable difference is seen for $F_2^{\mu n}/F_2^{\mu p}$ while the best fit to the points in fig. 5.6 is always obtained with $\delta = 1$.

5.2 Drell-Yan processes.

Drell-Yan processes in proton-nucleon and proton-proton collisions are very interesting because the theoretical predictions depend crucially on the antiquark content of the nucleons. In fig. 5.7 we compare the experimental data at the two different values of the center of mass energy $\sqrt{s} = 27.4$ GeV (fixed target at FNAL) [18] and $\sqrt{s} = 62$ GeV (ISR) [19,20] with the predictions obtained using our parametrizations (solid curves)*. The computation of the cross section includes the corrections of order α_s. To check the sensitivity of the results on the shape of the antiquark density we varied the power in $(1-x)$ (cfr. eq. (4.8)) between 6 and 9.5. The corresponding results (dashed curves) are also reported in the figure. We recall that the result of our fit to deep inelastic data gave:

$$\bar{q}(x, Q_0^2) \propto (1-x)^{8.5}$$

This choice appears to reproduce very well the experimental data. The agreement in shape with the experimental results is even more significative at $\sqrt{s} = 27.4$ GeV, where highest values in x are probed.

5.3 Parton densities from the two jets cross section.

To a good degree of accuracy the differential two jet cross section in $p\bar{p}$ processes can

---

* This analysis has already been performed in ref. [36].

be written as:

$$\frac{d^3\sigma}{dx_1 dx_2 d\cos\theta} \sim \frac{F(x_1)}{x_1}\frac{F(x_2)}{x_2}\frac{d\sigma}{d\cos\theta} \tag{5.1}$$

Where $F(x)$ is the combination [37]:

$$F(x) = G(x) + \frac{4}{9}(\bar{q}(x) + q(x)) \tag{5.2}$$

The typical scale at which the partons are probed is of the order of the invariant mass (or transverse momentum) of the two jet system ($Q^2 \sim 2000$ GeV^2) i.e. much higher than the reference scale at which the parton densities are measured in deep inelastic scattering.

In fig. 5.8 we show $F(x,Q^2)$ from the measurement of the UA1 collaboration [38,39] at the CERN $Sp\bar{p}S$ Collider, compared with our theoretical predictions.

5.4 Single photon production in $p\bar{p}$ processes.

In fig. 5.9 we report the data from the UA2 collaboration [40] together with the theoretical predictions obtained using our parton densities. Next to leading corrections have also been included [41] *.

5.5 W and Z^0 production cross sections and neutrino counting.

In fig. 5.10 we report the experimental W and Z^0 production cross sections times the branching ratio in $e\nu$ and e^+e^- respectively at $\sqrt{s} = 546$ and 630 GeV [42]. The curves are the predictions obtained using our parton parametrizations; the dashed areas represent the estimated theoretical uncertainty discussed in [43].

In table (5.1) the W and Z^0 production cross sections obtained using the present parton parametrizations in the range $\sqrt{s} = 0.546 \div 40.0$ TeV are also reported.

The ratio

$$R = \frac{\sigma^W B(W \to e\nu)}{\sigma^Z B(Z \to ee)} \tag{5.3}$$

is related both to the number of light neutrino families and to the top quark mass as first discussed in [44]. A comparison of the experimental results with the theoretical prediction

---

* We thank P. Aurenche who provided to us the computer program and for many illuminating discussions.

on R allows to derive some considerations on m_t and to calculate an upper limit on the additional number of neutrino flavours. The major source of error on the theoretical prediction comes from the use of structure functions in the calculation of $R' = \frac{\sigma^W}{\sigma^Z}$ even if most of the uncertainties which affect the absolute value of $\sigma^{W,Z}$ cancel out.

We estimate

$$R' = 3.28 \pm 0.15 \tag{5.4}$$

where the error comes mainly from the uncertainties on the valence quarks; those on the antiquark distribution and on $sin^2\theta_W$ are also taken into account. The error in eq. (5.4) is smaller than the error quoted in [45], which was obtained by comparing different parametrizations and not directly by evolving low energy deep inelastic data as we do here. In figs. (5.11) and (5.12) the ratio R is reported as a function of m_t together with the combined experimental results of UA1 and UA2 both at $\sqrt{s} = 546$ GeV and $\sqrt{s} = 630$ GeV [46] respectively for $N_\nu = 3$ and $N_\nu = 4$. The dashed line corresponds to the 95% upper limit derived from experimental results, the shaded region around the theoretical prediction for R represents the corresponding $\pm 1\sigma$ uncertainty belt. No conclusion on m_t can be drawn from the case $N_\nu = 3$ considering the actual experimental errors. On the contrary, considering the central theoretical prediction, the $N_\nu = 4$ case (fig. 5.12) brings to an upper bound for m_t of about 65 GeV at 95% c.l.

Finally in fig. 5.13 we report the 95% c.l. upper limit on ΔN_ν as a function of m_t that can be obtained using the combined data of UA1 and UA2 at $\sqrt{s} = 546$ GeV and $\sqrt{s} = 630$ GeV [46] and our prediction.

6. Parton densities at very high Q^2

This section is devoted to a detailed discussion of the parton densities evolved at scales much larger than $Q_0^2 = 10$ GeV^2. We study the indetermination of the parton densities at large scales standing from the errors (and differences among different experiments) in low energy measurements of structure functions. Then we compare our results with DO and EHLQ. Finally we show separately and comment the results of the leading and next to leading logarithmic evolution of the densities, obtained using our definition beyond the leading order (cfr. sect.2). The discussion on these points is important to monitor the error involved in theoretical predictions for cross sections at Super Collider energies. If not stated otherwise all figures refer to distributions evolved using only the lowest order Altarelli-Parisi kernels.

As described in sect.4.2 we have derived for valence quarks hard distribution (from BEBC data), a soft distribution (from CHARM data) and an average one. In fig. 6.1 we show the valence distribution $x(u_v(x) + d_v(x))$ in these three cases at $Q^2 = 10^4$ GeV^2 (intermediate vector boson scale) together with the corresponding curves obtained by DO and EHLQ. We see that the difference among the three different input distributions becomes smaller at higher scales.

In the case of the antiquark density there are two main sources of error. The first one comes directly from the measurement error on the overall normalization discussed in sect. 4.3; the second derives from the effect of $q\bar{q}$ pairs due to different initial gluon distributions. Since it is not possible to reconcile the CHARM and CDHS determination for the gluon we give separately in fig. 6.2 curves for $x\bar{q} = x\bar{u} + x\bar{d} + x\bar{s}$ corresponding to the gluon distribution from CDHS and the band obtained by varying the input gluon distribution within the confidence belt of the CHARM results. We also show in fig. 6.3 $x\bar{q}$ obtained in the extreme case in which the gluon distribution is fixed to zero at the initial scale Q_0^2 as a test of the importance of the gluon density in the evolution of the antiquarks.

In fig. (6.4) we report the gluon distribution at $Q^2 = 10^4$ GeV, derived from the band given by the three input gluon densities discussed in sec. (4). The results from the parametrization by DO and EHLQ are also given. The differences are reduced by the evolution: the distribution EHLQ is very similar with the hard gluon and the one from DO is contained in our band. For very small x the distribution determined by DO shows an unphysical growth; this is not surprising since the authors limit the validity of their parametrizations at $x = 10^{-3}$. In fig. (6.5) we also compare our results with those obtained by using at the input scale the gluon of CDHS. The difference observed at the reference scale (see fig. 4.3) is shifted down to smaller values of x but it is still present.

For the heavy flavour distributions (charm, bottom and top quarks) we assume that they are generated by the evolution process in QCD perturbation theory at the threshold $Q_f^2 = m_f^2$ as recently suggested in [4]. This relation is probably not appropriate beyond the leading logarithmic approximation. In any case we do not pretend to be able to describe the production of heavy quarks near the threshold or to be accurate beyond the LLA for these densities. We only want to have reasonable predictions at scales $Q^2 \gg m_f^2$. In fig. 6.6 we show the bottom and top distributions at $Q^2 = 10^6$ GeV^2 assuming $m_b = 4.5$ GeV and $m_t = 40$ GeV. By changing the physical threshold from m_f^2 to $4m_f^2$ we have found a variation of about 30% at most for the top density at $Q^2 = 10^6$ GeV^2. The effect we find on the second moment of the gluon is at most of $\sim 7\%$; this result is at variance with the numerical results of [4].

We have already discussed in detail the difference between our parametrizations and those by DO and EHLQ at low energy. To compare them at large scales we consider, following [3], the partonic luminosities

$$\frac{\tau d\mathcal{L}_{p_i p_j}}{d\tau} = \tau \int_\tau^1 \frac{dx}{x} [p_i(x) p_j(\frac{\tau}{x})] \qquad (6.1)$$

for the following combinations of densities:

$$\begin{aligned} gg &= G(x)G(\frac{\tau}{x}) \\ qq &= [u_v(x) + \overline{u}(x)][u_v(\frac{\tau}{x}) + \overline{u}(\frac{\tau}{x})] + (u \to d) + 2\overline{u}(x)\overline{u}(\frac{\tau}{x}) \\ qg &= 2[u_v(x) + d_v(x) + 2\overline{u}(x)]G(\frac{\tau}{x}) \\ u\overline{u} &= 2[u_v(x) + \overline{u}(x)]\overline{u}(\frac{\tau}{x}) \\ d\overline{d} &= 2[d_v(x) + \overline{d}(x)]\overline{d}(\frac{\tau}{x}) \end{aligned} \qquad (6.2)$$

In fig. 6.7 we give our results in pp collisions at $Q^2 = 10^6$ GeV^2. In figs. 6.8a, 6.8b, 6.9a and 6.9b we compare as an example the results obtained for the luminosities $\tau d\mathcal{L}_{qq}/d\tau$ and $\tau d\mathcal{L}_{gg}/d\tau$ together with those of DO and EHLQ.

We finally consider the effects of the next to leading corrections on the evolution. The effect is very tiny for valence quarks and we will not show the corresponding figure.

In figs. 6.10 and 6.11 we report instead the results of antiquark and gluon distributions evolved at $Q^2 = 10^4$ GeV^2 using the leading and next to leading order QCD formulae of sect. 2. The effect of the coefficient functions is, with our choice, very small and the correction is mostly due to the anomalous dimension. The two loop corrections become important in the very low x region which is relevant only in the production of relatively light objects (as is the case for W's and Z^0's at Super Collider energies) and at very large (positive or negative) values of the rapidity.

Appendix

A) The fast interpolating routines

A set of routines which produces the value of any parton density at a point in x, Q^2 requested by the user is provided. The value is the results of a two-dimensional interpolation in the x, Q^2 plane.

The routines provided are one for each foreseen case:

FXAVER with the results from average valence density, average CHARM gluon, evolution at leading order (LO)

FXVSOF the same, soft valence density, LO

FXVHAR the same, hard valence density, LO

FXGSOF the same, soft gluon density, LO

FXGHAR the same, hard gluon density, LO

FXCDGL with the results from average valence density, CDHS gluon, LO

FXNLLA with the results from average valence density, average CHARM gluon, evolution performed at next-to-leading order.

All the routines have the same structure and are called in the same way. They have three arguments of input and one of output:

FXAVER (X,Q2,STRFU,VAL) where

X is the value of x $(5 \cdot 10^{-5} \div 0.95)$ (real variable)

Q2 is the value of Q^2 $(10 \div 10^8)$ GeV^2 (real variable)

STRFU is the desired parton density (character variable) to be chosen amongst:

'UPVAL'	u_v quark distribution
'DOVAL'	d_v quark distribution
'GLUON'	G distribution
'QBAR '	$\bar{q}$ distribution
'UBAR '	$\bar{u}(=\bar{d})$ distribution
'SBAR '	$s(=\bar{s})$ distribution
'CBAR '	$c(=\bar{c})$ distribution
'BBAR '	$b(=\bar{b})$ distribution

'TBAR ' $t(=\bar{t})$ distribution.

VAL is the return argument containing the interpolated value.

Protections are put in such a way that values outside boundaries or negligibly small are set to zero.

B) The FORTRAN code

The FORTRAN code of the program that generates the parton densities at a given Q^2, starting from their Mellin transform at a reference Q_0^2 value is also available, and is maintained under PATCHY to ensure full portability. The code is designed in order to provide the user with a complete control of the inputs for the evolution, at three different levels:

a) To change the run parameters, as the scale Q^2, the interval in x, the value of Λ_{QCD}, etc.

b) To change the parameters of the densities, keeping the functional form given in the text.

c) To change even the functional form of the densities, providing the Mellin transform to the program.

The PAM file is organized in 3 patches: RUNDATA, PARTOSEQ and EVOL2. The patch EVOL2 contains the hard structure of the program and should never be modified by the user.

The variables controlling a specific run are defined in the RUNDATA patch, in form of DATA statements:

LOOPEV = 1 or 2 sets the calculations to one or two loops.

Q2IN defines the reference Q^2 scale in GeV for the input parton densities.

Q2FIN is the Q^2 value at which the parton densities are computed.

NPOINX is the number of points in x from XMIN to XMAX. According to the value of OPTION the intervals are equally spaced in x (OPTION=1) or in $\ln x$ (OPTION=2).

The charm, bottom and top masses are defined by MASCH, MASBO, MASTO, and ETA defines the corresponding threshold values, Q_f^2 according to the formula $Q_f^2 = \eta \cdot m_f^2$.

Finally, the Λ_{QCD} is defined by LAMBDA.

This way of defining all the parameters by DATA statements makes the resulting program entirely self consistent, not requiring any external file to be read. However a special dummy sequence called READPAR is also provided to allow the user to define, if needed, his/her own way to input the run parameters from a file, a terminal etc.

In the same patch another dummy sequence, called WRITEOUT, is also defined. It is called at the end of the program and can be replaced by user code to write out an output file, containing the parton density distributions at the final scale, in a format suitable for subsequent use. The user has just to know that the distributions are contained in the array PARTON (N,I), with N=1,NPOINX and I=1,9 with the following meaning:

I = 1 u_v quark distribution
I = 2 d_v quark distribution
I = 3 G distribution
I = 4 $\bar{q}$ distribution
I = 5 $\bar{u}(=\bar{d})$ distribution
I = 6 $s(=\bar{s})$ distribution
I = 7 $c(=\bar{c})$ distribution
I = 8 $b(=\bar{b})$ distribution
I = 9 $t(=\bar{t})$ distribution.

The NPOINX x values are stored in the array XX(NPOINX).

The sequences defining the input parton distributions are contained in the patch PARTOSEQ. The user can operate at two different levels: the simplest one is to change the parameters keeping the functional definition of the densities. The parameters are contained in the sequence PARTPAR, where the parameter names are such so as to translate the text formulae in the following FORTRAN expressions:

eq. (4.4) divided by x, describing u_v:

```
AA*X**ALF*(1-X)**BETA*(1+APIC*(1-X)+BPIC*(1-X)**2+CPIC*(1-X)**3)
```

eq. (4.1), d_v/u_v:

```
RPIC*(1-X)
```

eq. (4.8), $x \cdot (\bar{u} + \bar{d} + \bar{s})$:

```
XAAM*(1-X)**BETM*(1+XAPIM*X+XBPIM*X**2+XCPIM*X**3)
```

For the gluon two alternatives are foreseen, corresponding to the fits respectively to the CHARM data and to the CDHS data. The latter form, where xG is given by eq. (4.10), is translated into:

```
A1GL*(1-X)**B1GL*(1+AG1*X).
```

The fit to CHARM data is given directly in the Mellin space by the equation (4.9), with the following correspondence between symbols and variables:

A: AGL, α: ALFGL, β: BETGL, δ: DELGL.

The choice is made activating one of the two sequences:

```
+KEEP,GLUON,IF=CHARMGLU
```

or

```
+KEEP,GLUON,IF=EXPGLU,IF=-CHARMGLU.
```

the CHARM fit is then selected by default, with a cradle like:

```
+USE.
+EXE.
```

The exponential form can be selected by

```
+USE.
+USE,CHARMGLU,T=INHIBIT.
+EXE.
```

or, alternatively, by

```
+USE,RUNDATA,PARTOSEQ,EVOL2,EXPGLU.
+EXE.
```

A deeper modification of the parton densities can be obtained directly changing the definition of their Mellin transforms. The default code is contained in the sequences UPVAL, DOVAL, QQBAR (and QQBARI) and GLUON respectively for u_v, d_v, $x \cdot (\bar{u} + \bar{d} + \bar{s})$ and xG. The rules to be strictly followed are the following:

1) The Mellin trasform must be put at the end of the sequence in the variables UPVAL, DOVAL, QQBAR, and GLUEN respectively.
2) The user FORTRAN parameters must go in the commons PARVAL, PARQUB and PARGLU, that are placed in the same patch.
3) These parameters must be defined in PARTPAR or read in READPAR, with the

same rules as given before.

4) The printout of the parameters, contained in the sequence PRINPART in the same patch, must be modified accordingly.

REFERENCES

1. J.F. Owens and E. Reya, Phys. Rev. D17 (1978) 3003.
   R. Baier, J. Engels and B. Petersson, Z. f. Phys. C2 (1979) 265.
   M. Glück, E. Hoffmann and E. Reya, Z. f. Phys. C13 (1982) 119.
2. D.W. Duke and J.F. Owens, Phys. Rev. D30 (1984) 49.
3. E. Eichten, I. Hinchliffe, K. Lane and C. Quigg, Rev. Mod. Phys. 56 (1984).
4. J.C. Collins and D.E. Soper, Nucl. Phys. B194 (1982) 445.
   J.C. Collins and W.K. Tung, Nucl. Phys. B278 (1986) 934.
5. G. Altarelli, R. K. Ellis, G. Martinelli, Nucl. Phys. B143 (1978) 521; B146 (1978) 544; B157 (1979) 461.
6. J. Kubar-Andre, F. E. Paige, Phys. Rev. D19 (1979) 221.
7. M. Diemoz, F. Ferroni, E. Longo, Phys. Rep. 130 (1986) 293.
8. W. Furmanski and R. Petronzio, Z. f. Phys. C11 (1982) 293.
9. I. Hinchliffe and C. H. Llewellyn Smith, Nucl. Phys. B143 (1978) 521
10. E.G. Floratos et al., Nucl. Phys. B192 (1981) 417.
11. J.J. Aubert et al., Nucl. Phys. B259 (1985) 189.
12. J.J. Aubert et al., Nucl. Phys. B272 (1986) 158.
13. M. Virchaux, Proc. XXIII Int. Conf. on High Energy Physics, Berkeley 1986.
14. D. Allasia et al., Z. f. Phys. C28 (1985) 321.
15. D.B. MacFarlane et al., Fermilab-pub-83/108-Exp (1983).
16. H. Abramowicz et al., Z. f. Phys. C17 (1983) 237.
17. F. Bergsma et al., Phys. Lett. 123B (1983) 269.
18. A. S. Ito et al., Phys. Rev. D23 (1981) 604.
19. C. Kourkoumelis et al., Phys. Lett. 91B (1980) 475.
20. A.L.S. Angelis et al., Phys. Lett. 147B (1984) 472.
21. D. Allasia et al., Phys. Lett. 135B (1984) 231.
22. H. Abramowicz et al., Z. f. Phys. C25 (1984) 29.

23. S.J. Brodsky, G. Farrar, Phys. Rev. Lett. 31 (1973) 1153; Phys. Rev. D12 (1979) 1309.
24. J.J. Aubert et al., Phys. Lett. 123B (1983) 275.
25. A. Bodek et al., Phys. Rev. Lett. 50 (1983) 1431. Phys. Rev. Lett. 51 (1983) 534.
26. R.G. Arnold et al., Phys. Rev. Lett. 52 (1984) 727.
27. A.C. Benvenuti et al., CERN-EP/87-13, 1987.
28. H. Abramowicz et al., Z. f. Phys. C15 (1982) 19.
29. M. Strovink, Lepton Photon Conference, Bonn (1981) 594.
30. H. Wachsmuth, CERN-EP/86-168, 1986.
31. Parametrization of proton structure functions, CHARM coll., to be published.
32. H. Abramowicz et al., Z. f. Phys. C12 (1982) 289.
33. P. R. Norton, Proc. XXIII Int. Conf. on High Energy Physics, Berkeley 1986.
34. J.J. Aubert et al., Phys. Lett. 123B (1983) 123.
35. A. Benvenuti, private communication.
36. G. Altarelli, R. K. Ellis, G. Martinelli, Phys. Lett. 151B (1985) 457.
37. F. Halzen, P. Hoyer, Phys. Lett., 130B (1983) 326.
38. G. Arnison et al., Phys. Lett. 136B (1984) 294.
39. F. Ceradini, Proc. XXIII Int. Conf. on High Energy Physics, Berkeley 1986.
40. J. A. Appel et al., CERN-EP/86-64.
41. P. Aurenche et al., Phys. Lett. 140B (1984) 87.
42. E. Locci, CERN-EP/86-159, 1986.
43. G. Altarelli, R. K. Ellis, G. Martinelli, Z. f. Phys. C27 (1985) 617.
44. N. Cabibbo, Proc. III Topical Workshop on $p\bar{p}$ Collider Physics, CERN 83-04, 1983.
45. F. Halzen, Phys. Lett. 182B (1986) 388.
46. D. Denegri, private communication.

FIGURE CAPTIONS

Fig. 4.1 The experimental points are the results from BEBC, CCFFRR, CDHS and CHARM at a $Q^2 \sim 10$ GeV^2 for the measurement of xF_3. The solid line is the best fit to all points. The dashed (dotted) curve represents the fit to CHARM (BEBC) only.

Fig. 4.2 The solid curve is the "average" valence distribution to leading order. The dashed curve includes our next to leading definition of the parton densities.

Fig. 4.3 The three solid curves are the soft, the hard and the central gluon distributions extracted from CHARM determination, the dashed one represents the result of CDHS.

Fig. 4.4 The soft, average and hard valence distributions (solid lines) used as input in this work are compared with DO (dashed line) and EHLQ (dotted line) at $Q_0^2 = 10$ GeV^2.

Fig. 4.5 The soft, average and hard gluon distributions (solid lines) used as input in this work are compared with DO (dashed line) and EHLQ (dotted line) at $Q_0^2 = 10$ GeV^2.

Fig. 4.6 The antiquark distribution shown with its uncertainty belt (solid lines) used as input in this work is compared with DO (dashed line) and EHLQ (dotted line) at $Q_0^2 = 10$ GeV^2.

Fig. 5.1 The experimental points are from ref.[11]; the solid curve has been obtained by using our "average" parton parametrizations from eqs.(4.4) and (4.8). The dashed and dotted curves have been obtained using the parametrizations of DO and EHLQ respectively.

Fig. 5.2 The experimental points are the same as in fig. (5.1). The solid curve has been derived using the "hard" valence quark parametrization (eq.(4.5)).

Fig. 5.3 $F_2^{\mu N}$ on a heavy target from ref.[12] compared with our "average" predictions (solid curve), DO (dashed curve) and EHLQ (dotted curve).

Fig. 5.4 Comparison of $F_2^{\mu n}/F_2^{\mu p}$ from refs.[33, 34] with the theoretical predictions: from the present analysis (solid curve), from DO (dashed curve) and EHLQ (dotted curve).

Fig. 5.5 Data from refs.[25, 26] (SLAC1 and SLAC2) and [33] (BCDMS) compared with the predictions obtained by using the DO parametrizations.

Fig. 5.6 The ratio d_v/u_v, measured in refs.[21] and [22] is compared with our predictions (solid curve), DO (dashed curve) and EHLQ (dotted curve).

Fig. 5.7 Lepton pair production at fixed target energies ($\sqrt{s} = 27.4$ GeV), (ref.[18]) and ISR energies ($\sqrt{s} = 62$ GeV), refs.[19, 20], are compared with our predictions (solid curves). Dashed curves a, b, c, d are the predictions obtained by assigning to the power of the term $(1 - x)$ of $\bar{q}$ respectively the values 6, 6.6, 7.5, 9.5.

Fig. 5.8 $F(x, Q^2)$ defined in eq. 5.2 as measured by the UA1 Collaboration [38, 39]. The dots are the points corresponding to a scale $Q^2 \sim 2000$ GeV^2. The squares are results obtained at a lower scale $Q^2 \sim 200$ GeV^2. The solid line has been derived using our parton densities evolved at $Q^2 = 2000$ GeV^2. The dashed line is the quark contribution alone. In the low x region the result is not very sensitive to scaling violations in the range $Q^2 = 200 - 2000$ GeV^2 as can be seen from the dotted curve representing $F(x)$ at $Q^2 = 200$ GeV^2.

Fig. 5.9 Single photon production in $\bar{p}p$ collisions at $\sqrt{s} = 630$ GeV. The data are from the UA2 collaboration, the solid curve has been obtained using our parton densities and the parton cross sections includes higher order corrections computed in ref.[40]. The scale for the running coupling constant and the parton densities has been chosen to be $p_T^2/2$.

Fig. 5.10 Experimental cross sections times branching ratios, $\sigma^W B^{e\nu}$ and $\sigma^Z B^{ee}$, are compared to our results. For these curves we have chosen $sin^2\theta_W = 0.229$, $M_W = 80.8$ GeV and $M_Z = 92$ GeV. The shaded area represents the uncertainty coming from the error on parton densities and on $sin^2\theta_W$, the ambiguity on the scale and of higher order terms contribution.

Fig. 5.11 The ratio $R = \sigma^W B^{e\nu}/\sigma^Z B^{ee}$ experimentally determined (UA1+UA2) (straight solid line) with its 95 % upper limit (dashed line) is compared to the theoretical expectation (shaded region) from our parametrization as a function of top quark mass for 3 neutrino families.

Fig. 5.12 The ratio $R = \sigma^W B^{e\nu}/\sigma^Z B^{ee}$ experimentally determined (UA1+UA2) (straight solid line) with its 95 % upper limit (dashed line) is compared to the theoretical expectation (shaded region) from our parametrization as a function of top quark mass for 4 neutrino families.

Fig. 5.13 The 95% c. l. upper limit on the additional number of light neutrino families obtained, as a function of the top quark mass, from the comparison of the experimentally determined value of R and our prediction. The allowed region is the one below the curve.

Fig. 6.1 Our soft, average and hard valence distributions (solid lines) evolved at $Q^2 = 10^4$ GeV^2 are compared with DO (dashed line) and EHLQ (dotted line) predictions.

Fig. 6.2 Antiquark distribution from average gluon (solid curve), soft gluon (dotted curve), hard gluon (dashed-dotted curve) and CDHS gluon (dashed curve).

Fig. 6.3 Our antiquark distribution at $Q^2 = 10^4$ GeV^2 (solid curve). The dashed curve represent the antiquark distribution in the case in which the gluon is assumed to be zero at the initial scale.

Fig. 6.4 Our soft, average and hard gluon distributions (solid curves) evolved at $Q^2 = 10^4$ GeV^2 are compared with DO (dashed curve) and EHLQ (dotted curve) predictions.

Fig. 6.5 Our soft, average and hard gluon distributions (solid lines) are compared with CDHS gluon distribution (dotted line) at $Q^2 = 10^4$ GeV^2 .

Fig. 6.6 Bottom (solid line) and top (dashed line) densities are shown for a threshold value $Q^2_{b,t} = m^2_{b,t}$ at $Q^2 = 10^6$ GeV^2.

Fig. 6.7 The luminosities relevant in pp collisions (eqs.(6.2)) computed using our parametrization are shown as a function of τ.

Fig. 6.8 The quark-quark luminosity computed using our parametrizations (solid curve) is compared to the one from EHLQ (dashed curve) and DO (dashed-dotted curve) in the range $10^{-5} \leq \tau \leq 0.25$ *(a)* and $10^{-4} \leq \tau \leq 10^{-2}$ *(b)*.

Fig. 6.9 The gluon-gluon luminosity computed using our parametrizations (solid curve) is compared to the one from EHLQ (dashed curve) and DO (dashed-dotted curve)in the range $10^{-5} \leq \tau \leq .25$ *(a)* and $5 \cdot 10^{-3} \leq \tau \leq 0.1$ *(b)*.

Fig. 6.10 Antiquark distribution from one loop (dashed curve) and two loop (solid curve) evolution at $Q^2 = 10^4$ GeV^2.

Fig. 6.11 Gluon distribution from one loop (dashed curve) and two loop (solid line) evolution at $Q^2 = 10^4$ GeV^2.

Tab. 3.1: Integration limits

	N-S	N-S	S	S
x	< 0.5	≥ 0.5	< 0.5	≥ 0.5
$\Re_0$	1	3	2	3
$\Re$	-14	3	-7	3
$\Im$	25	100	25	100

Tab. 5.1: *W* and *Z* cross sections

$\sqrt{s}$ (TeV)	σ^W (nb)	σ^Z (nb)
.54	4.3	1.3
.63	5.6	1.7
1.6	18	5.2
2.0	23	6.6
5.0	54	16
10	100	30
20	180	54
40	310	95

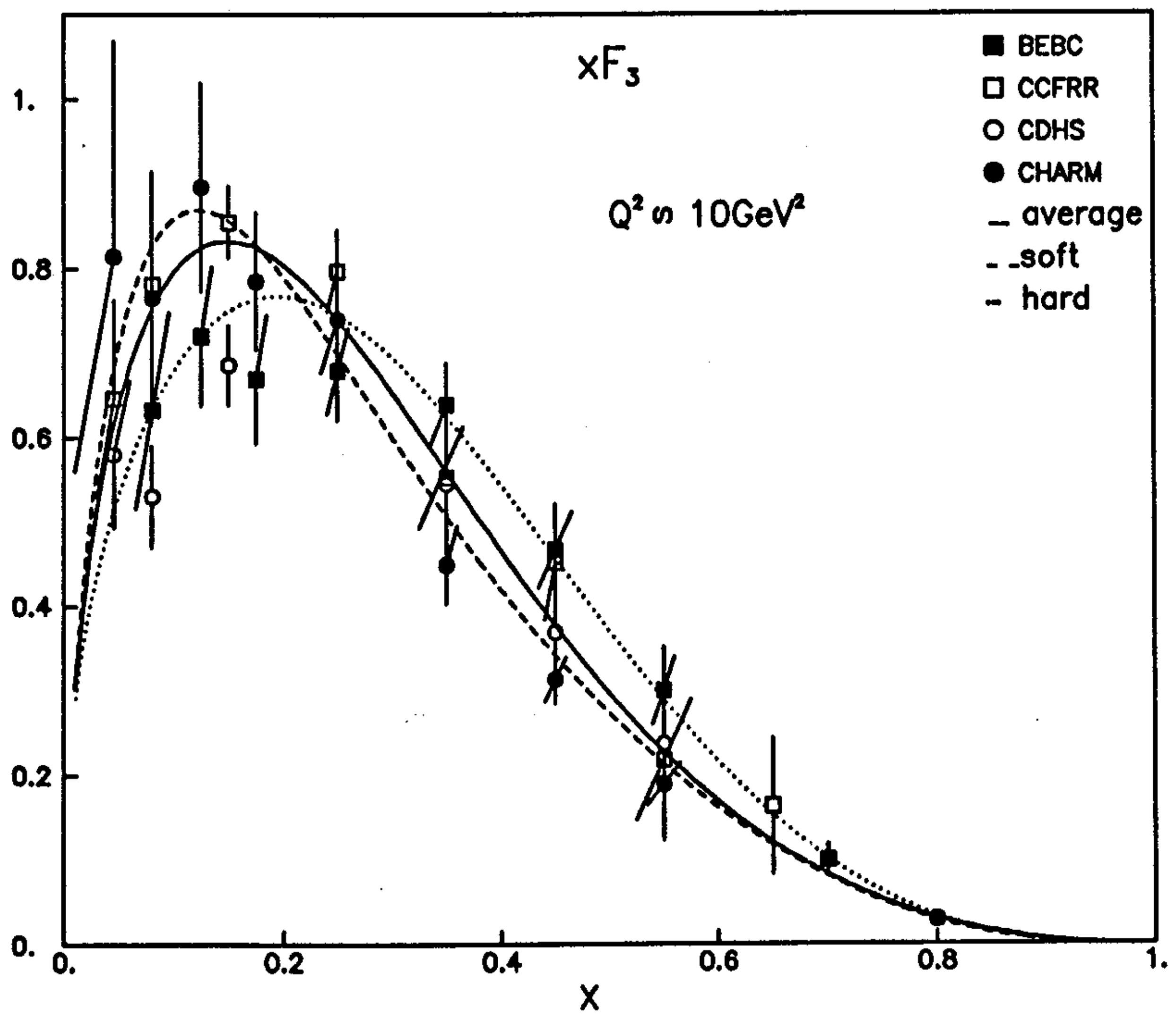
xF_3
$Q^2 \approx 10GeV^2$
■ BEBC
□ CCFRR
○ CDHS
● CHARM
— average
- - soft
·· hard
0.
0.2
0.4
0.6
0.8
1.
X

Fig. 4.1

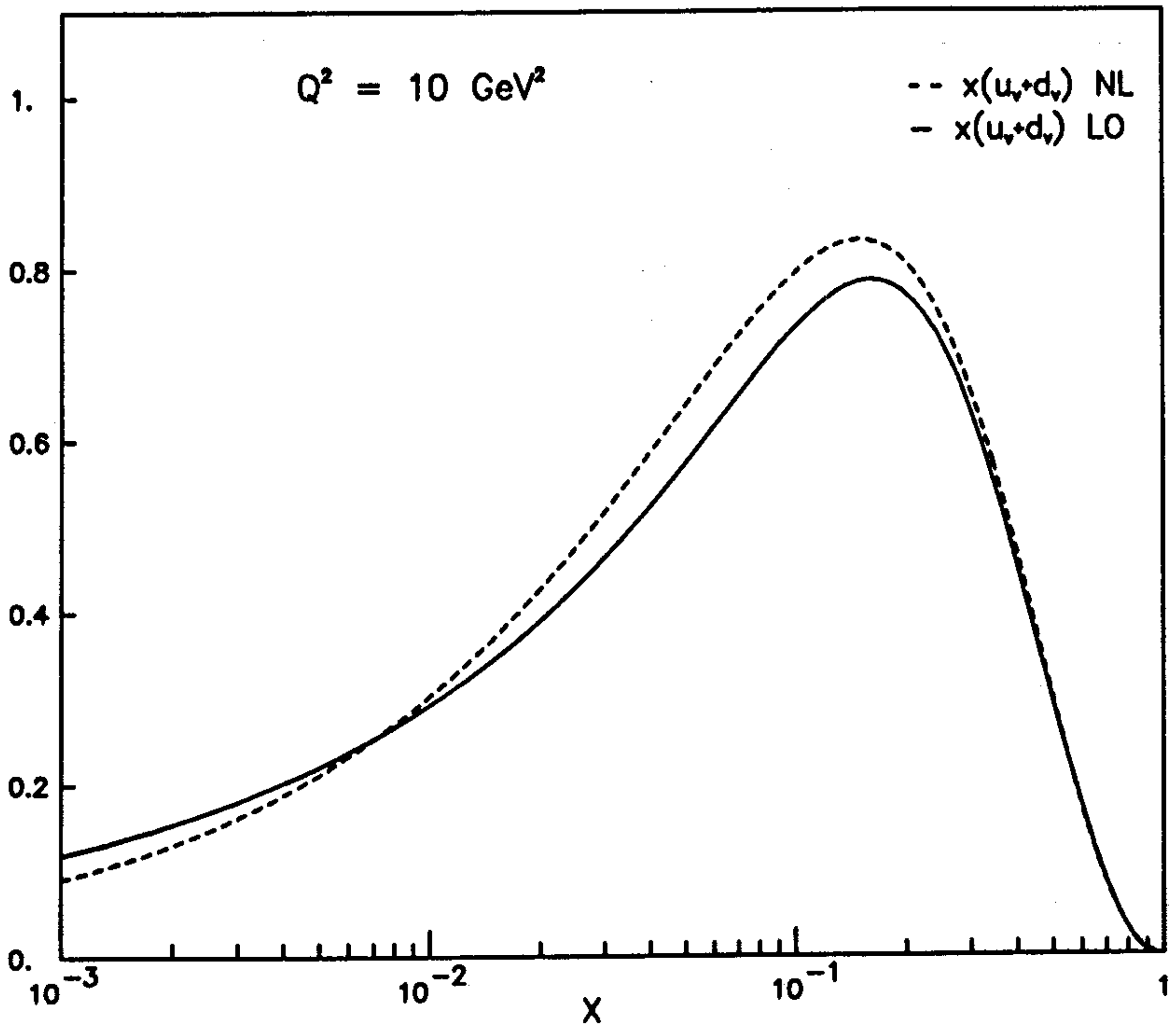

Fig. 4.2

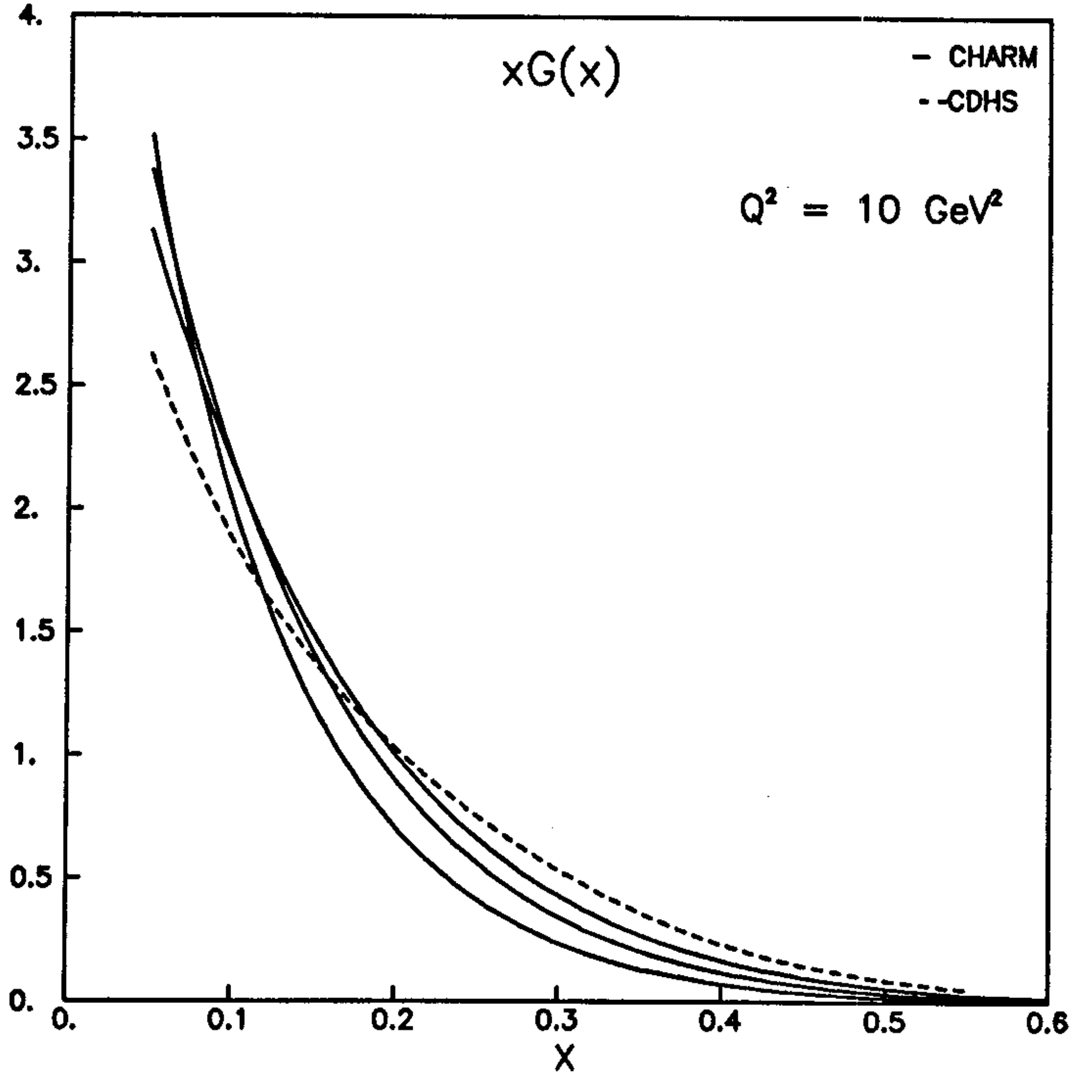
xG(x)
- CHARM
- -CDHS
$Q^2 = 10\ \mathrm{GeV}^2$
4.
3.5
3.
2.5
2.
1.5
1.
0.5
0.
0.
0.1
0.2
0.3
0.4
0.5
0.6
X

Fig. 4.3

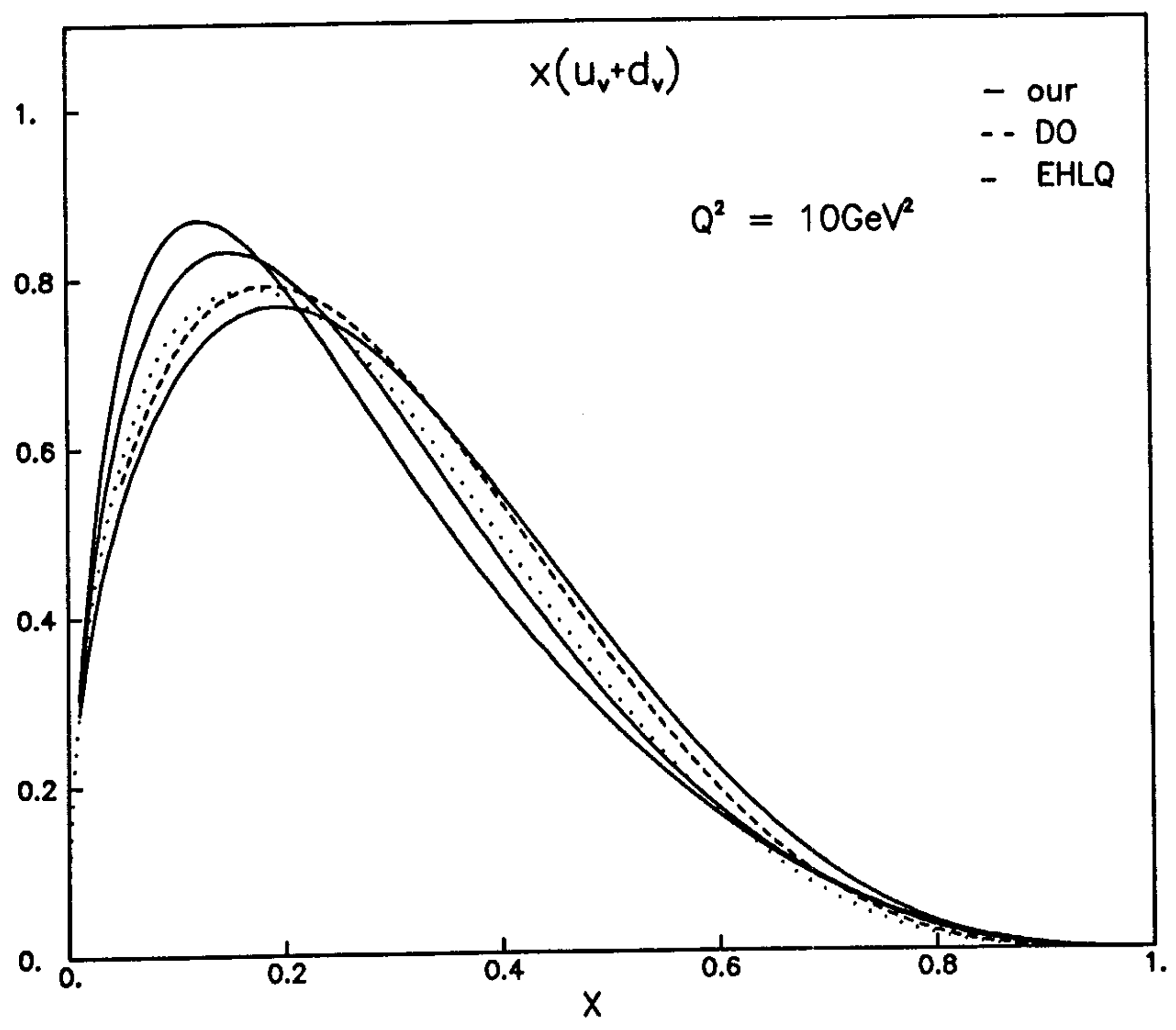

Fig. 4.4

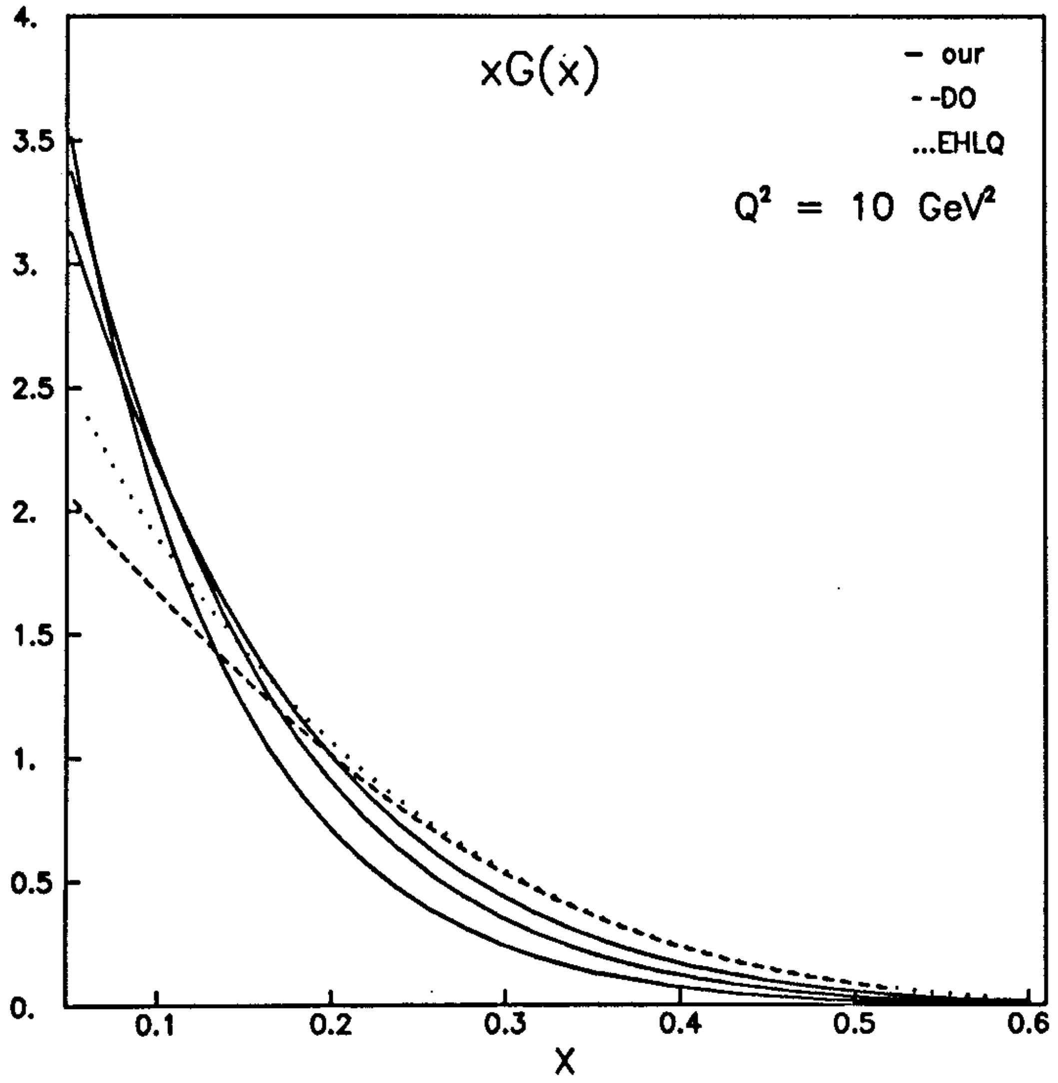

Fig. 4.5

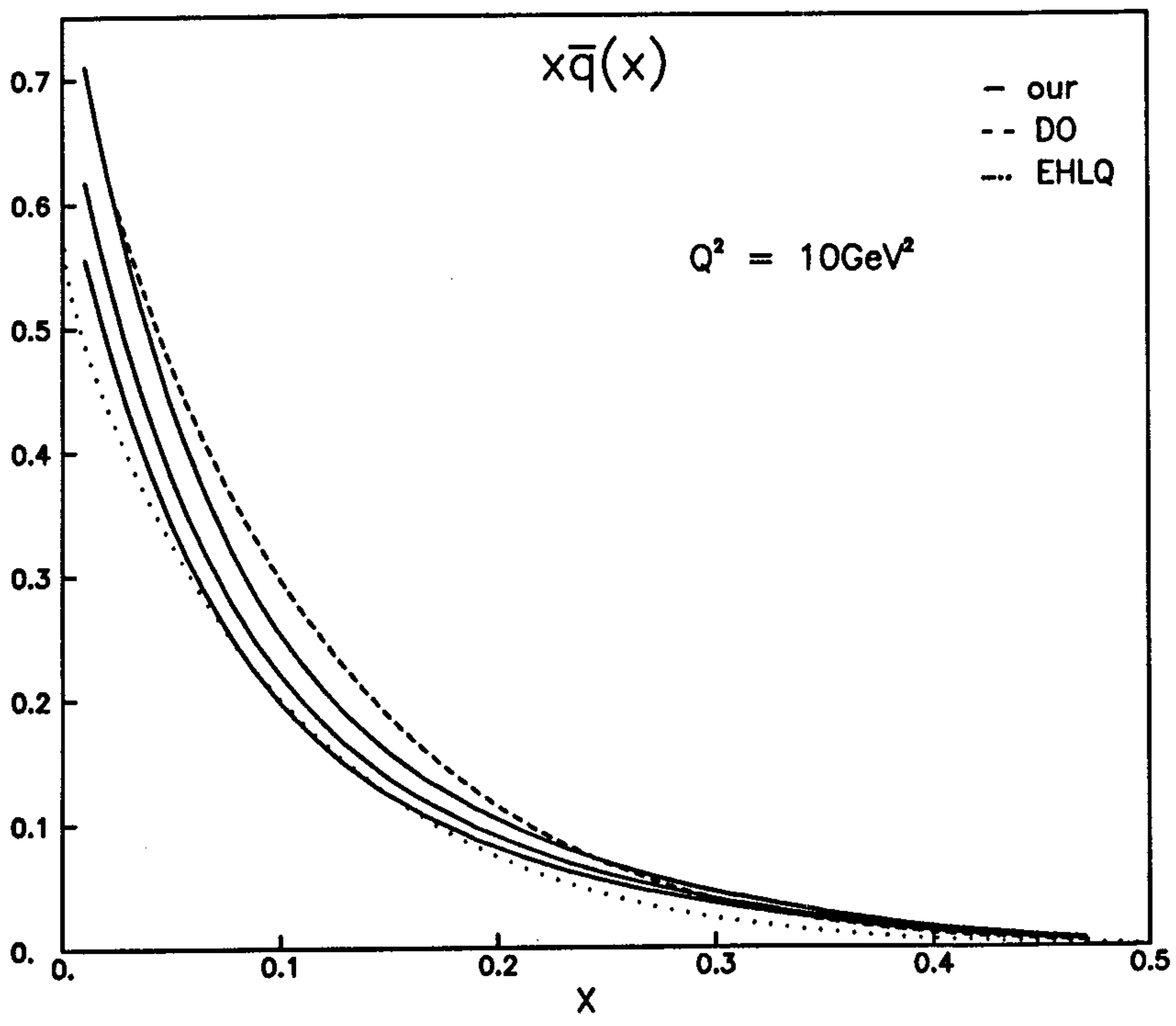
$x\bar{q}(x)$
— our
- - DO
.... EHLQ
$Q^2 = 10\mathrm{GeV}^2$
0.7
0.6
0.5
0.4
0.3
0.2
0.1
0.
0.
0.1
0.2
0.3
0.4
0.5
X

Fig. 4.6

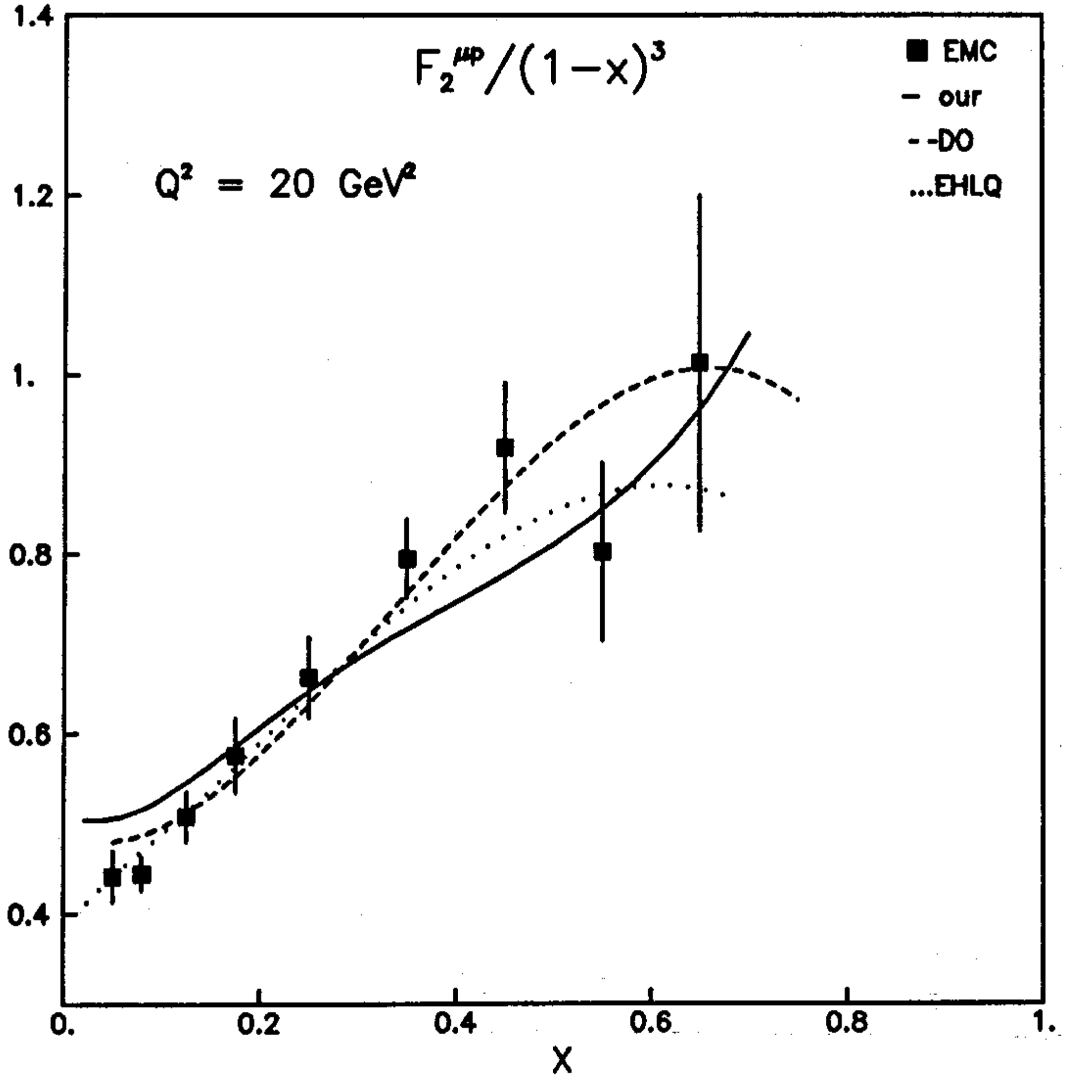
$F_2^{\mu p}/(1-x)^3$
$Q^2 = 20\ GeV^2$
■ EMC
– our
- -DO
...EHLQ
1.4
1.2
1.
0.8
0.6
0.4
0.
0.2
0.4
0.6
0.8
1.
X

Fig. 5.1

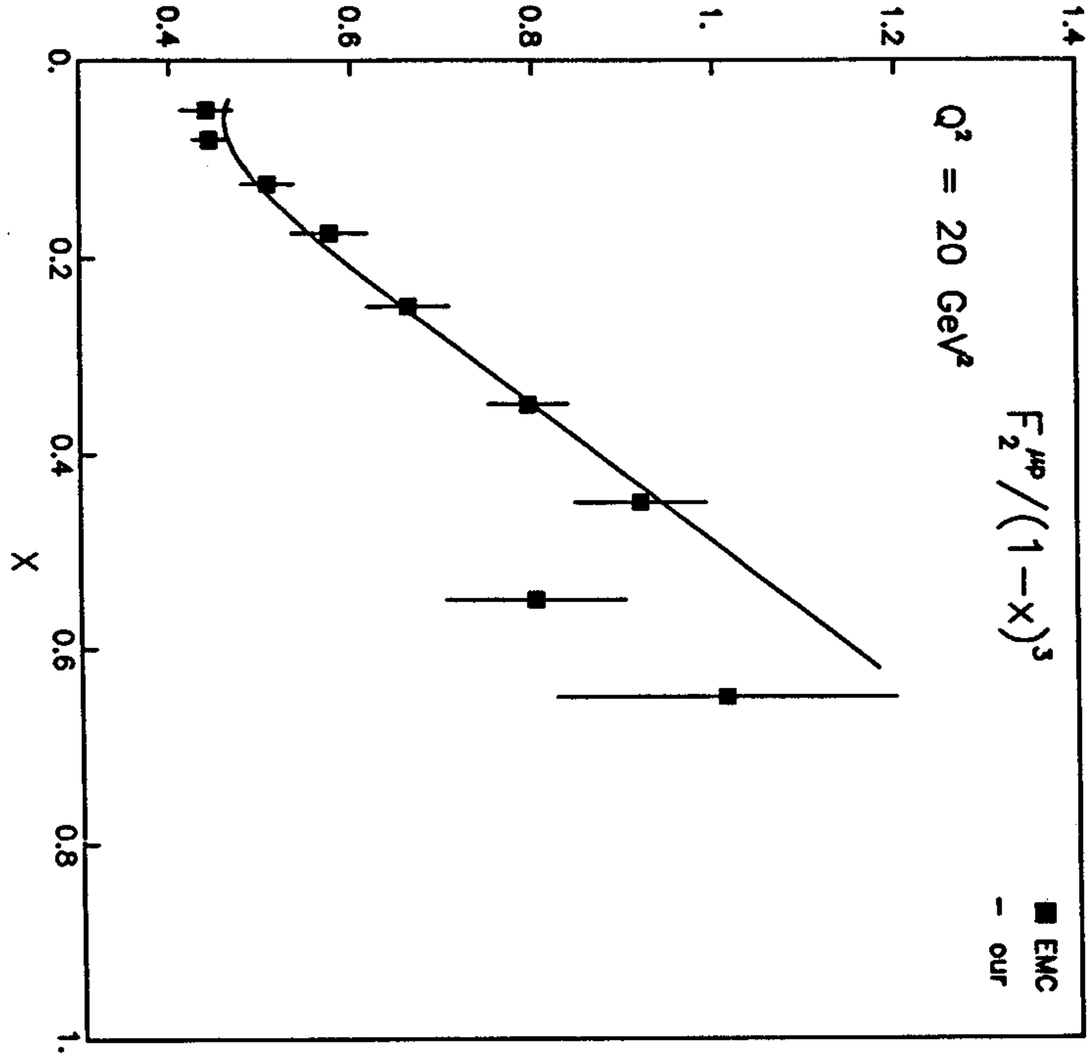

Fig. 5.2

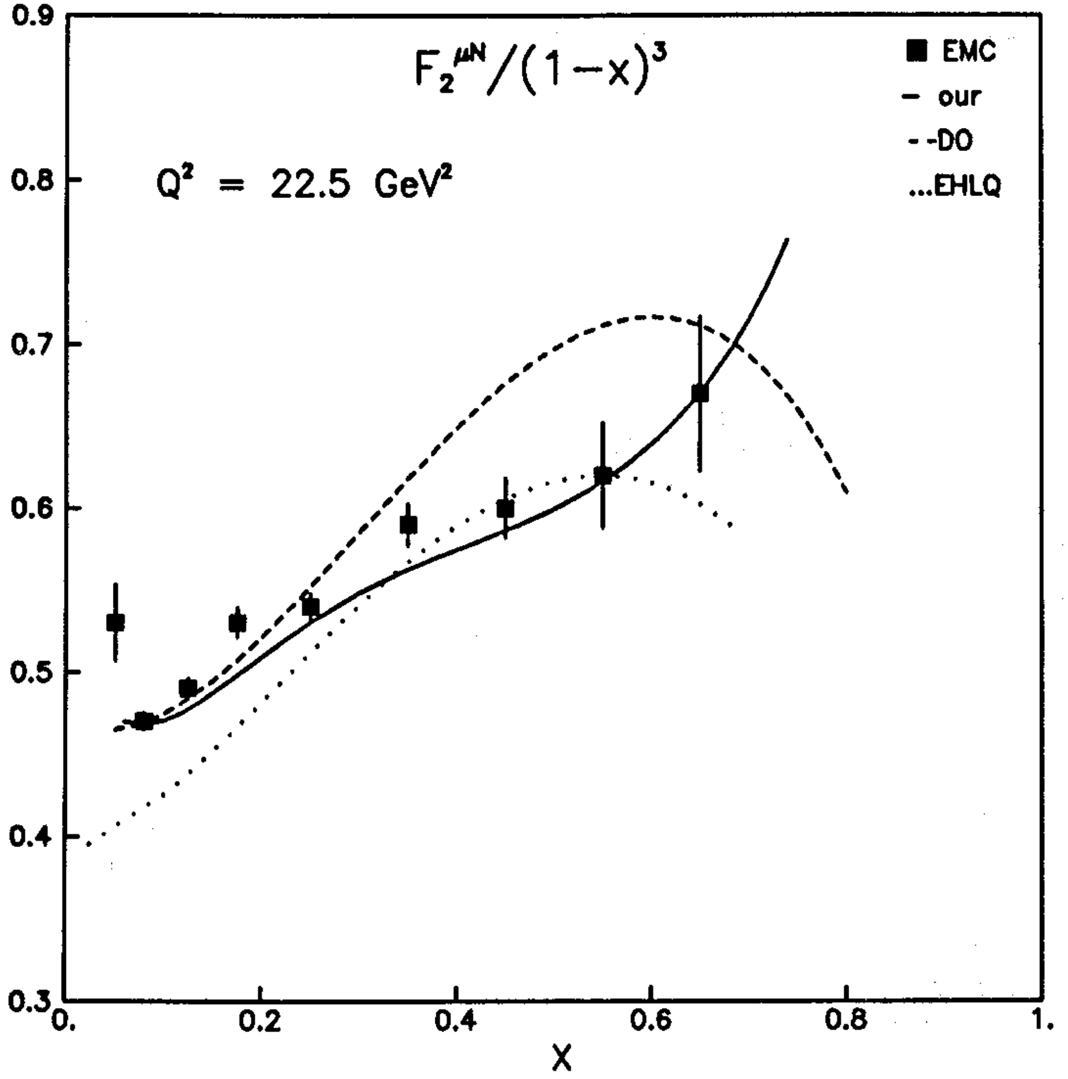

$F_2^{\mu N}/(1-x)^3$
$Q^2 = 22.5$ GeV^2
■ EMC
– our
- -DO
...EHLQ
0.9
0.8
0.7
0.6
0.5
0.4
0.3
0.
0.2
0.4
0.6
0.8
1.
X

Fig. 5.3

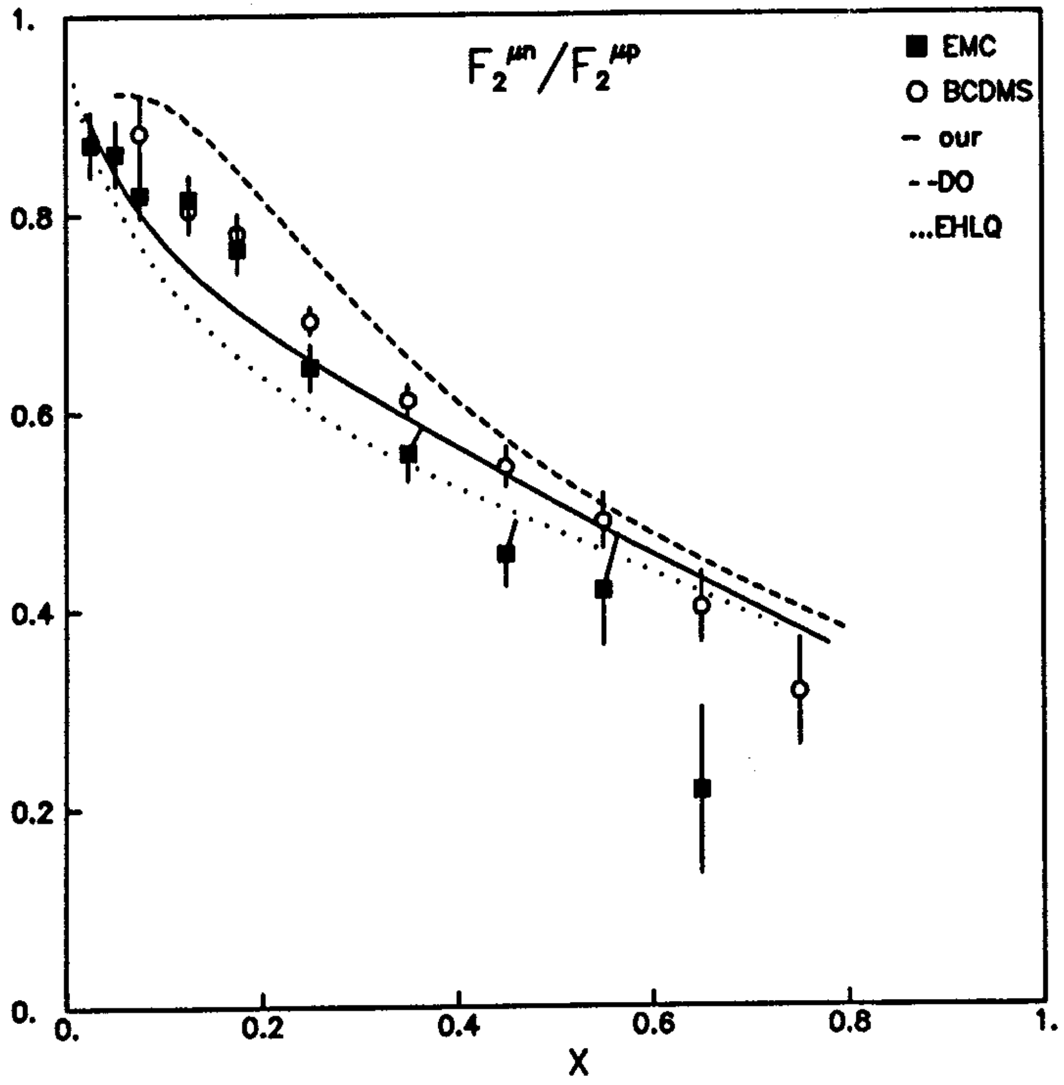

Fig. 5.4

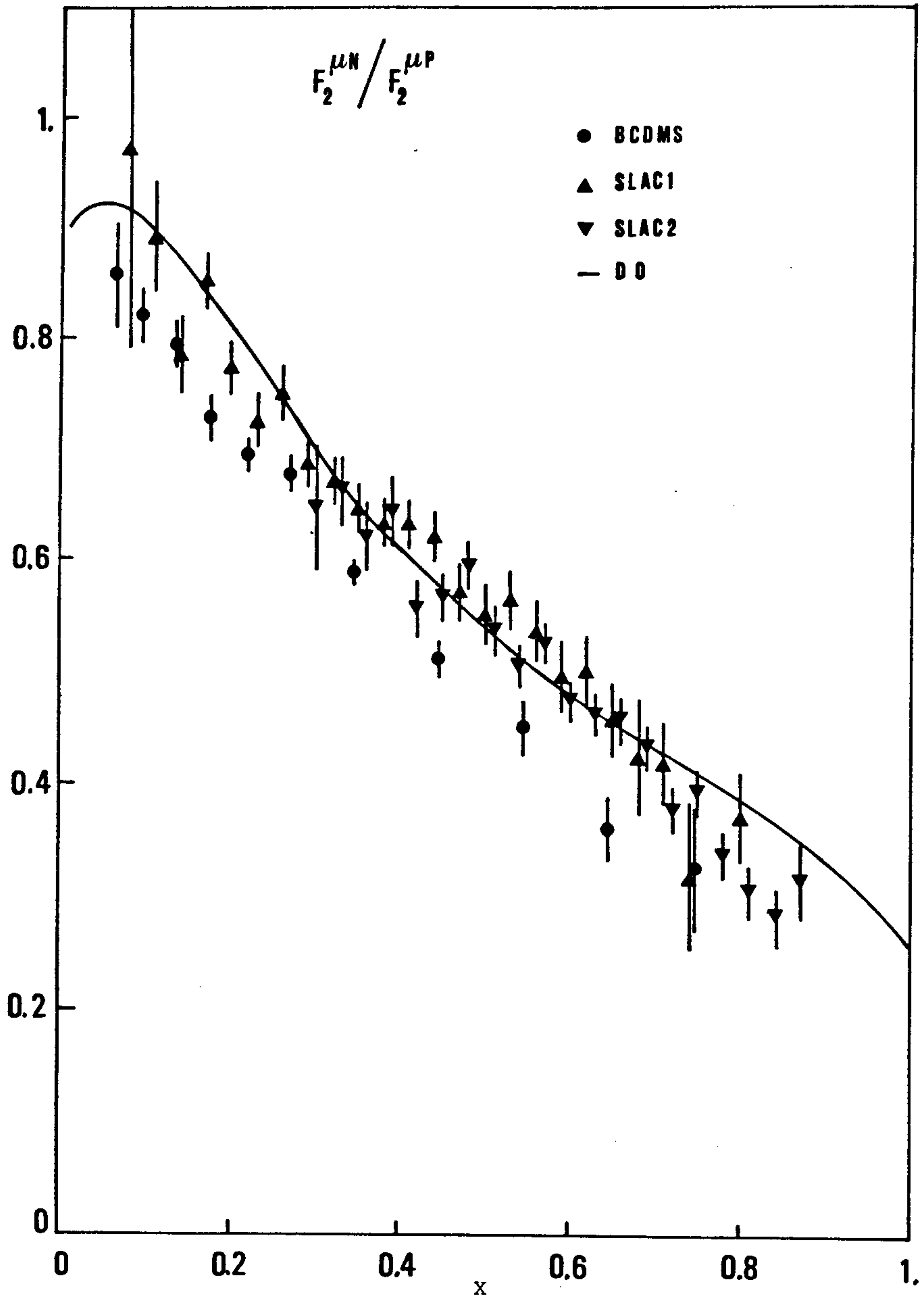

Fig. 5.5

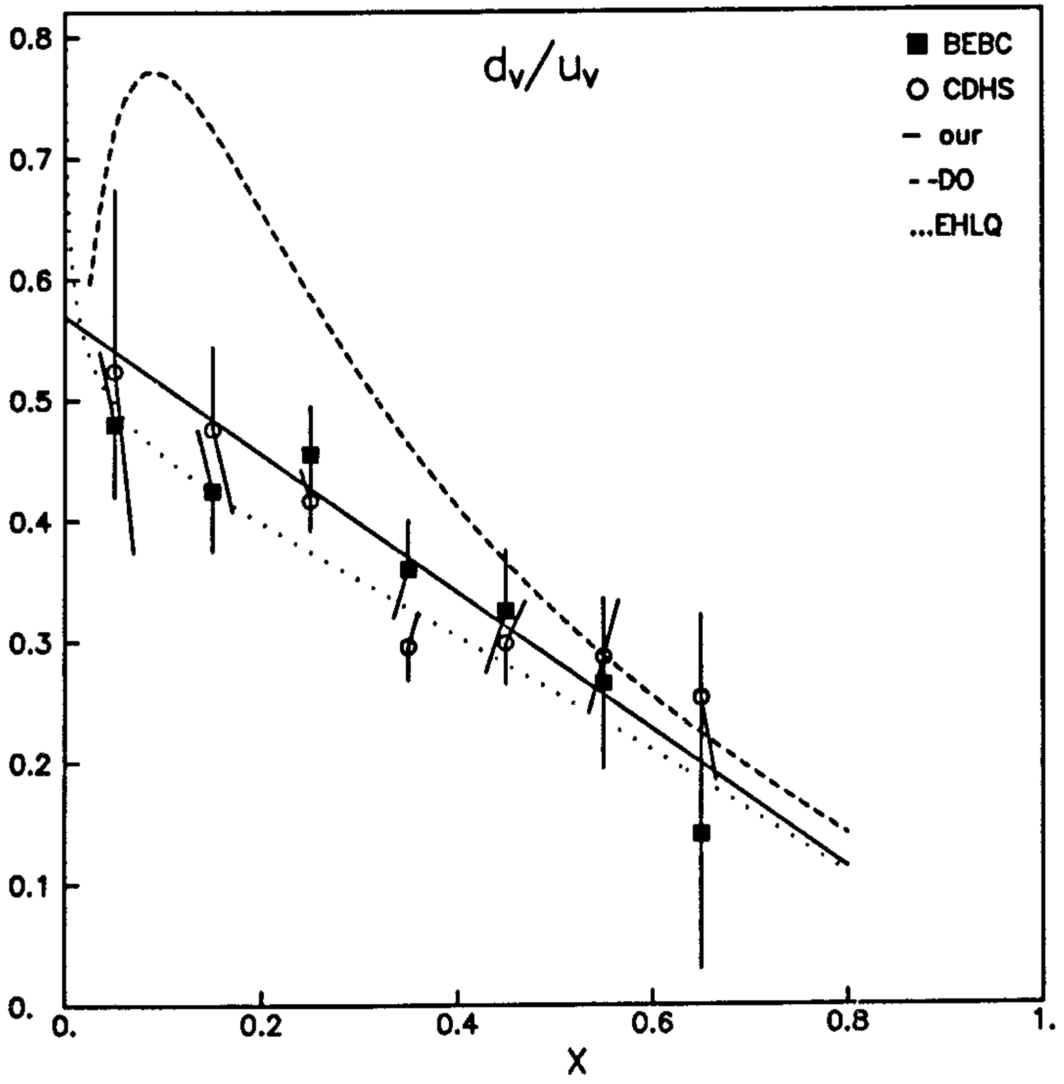

Fig. 5.6

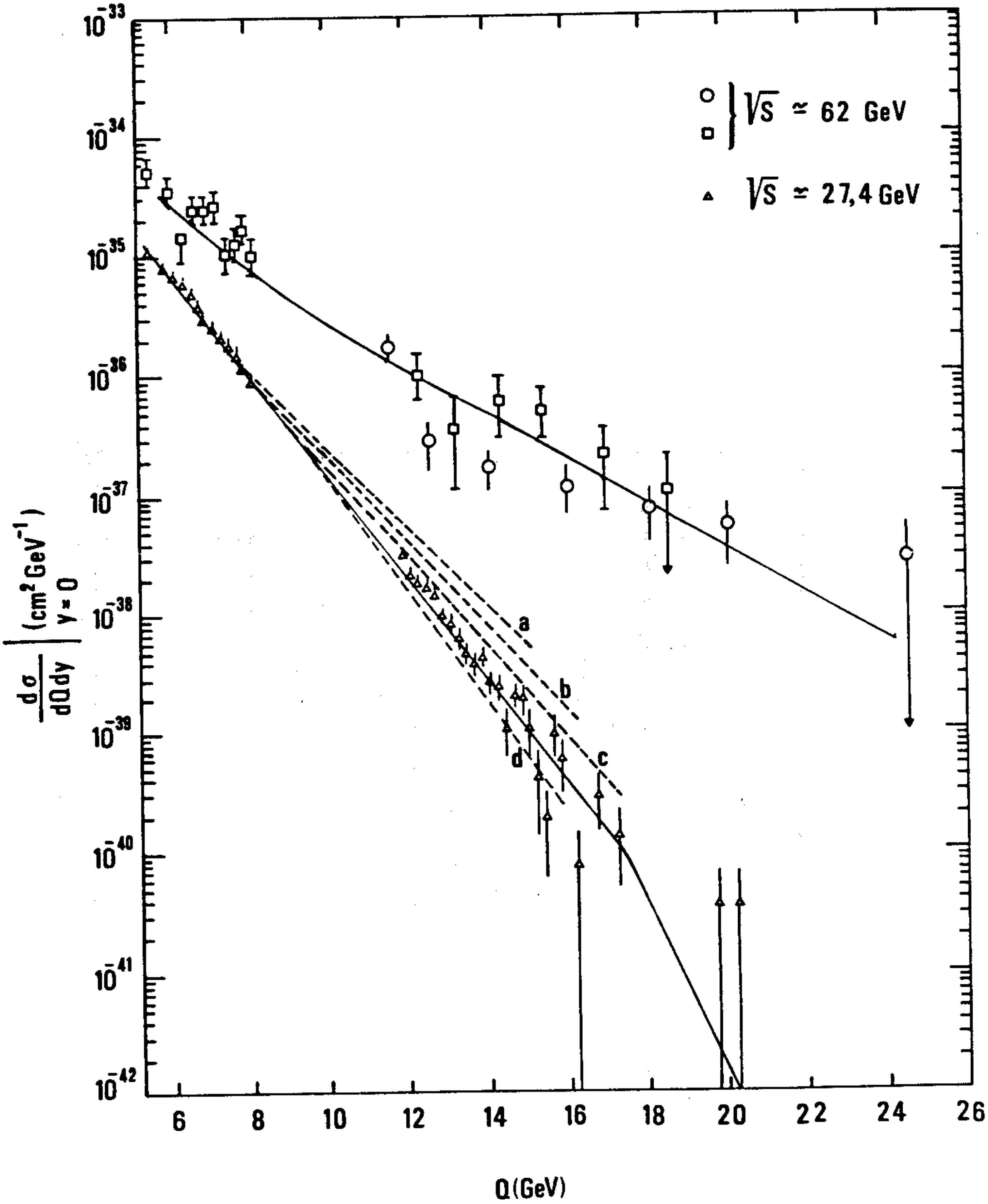
10^{-33}
10^{-34}
10^{-35}
10^{-36}
10^{-37}
10^{-38}
10^{-39}
10^{-40}
10^{-41}
10^{-42}
$\left.\frac{d\sigma}{dQdy}\right|_{y=0}$ $(cm^2 GeV^{-1})$
6
8
10
12
14
16
18
20
22
24
26
Q(GeV)
$\sqrt{S} \simeq 62$ GeV
$\sqrt{S} \simeq 27{,}4$ GeV
a
b
c
d

Fig. 5.7

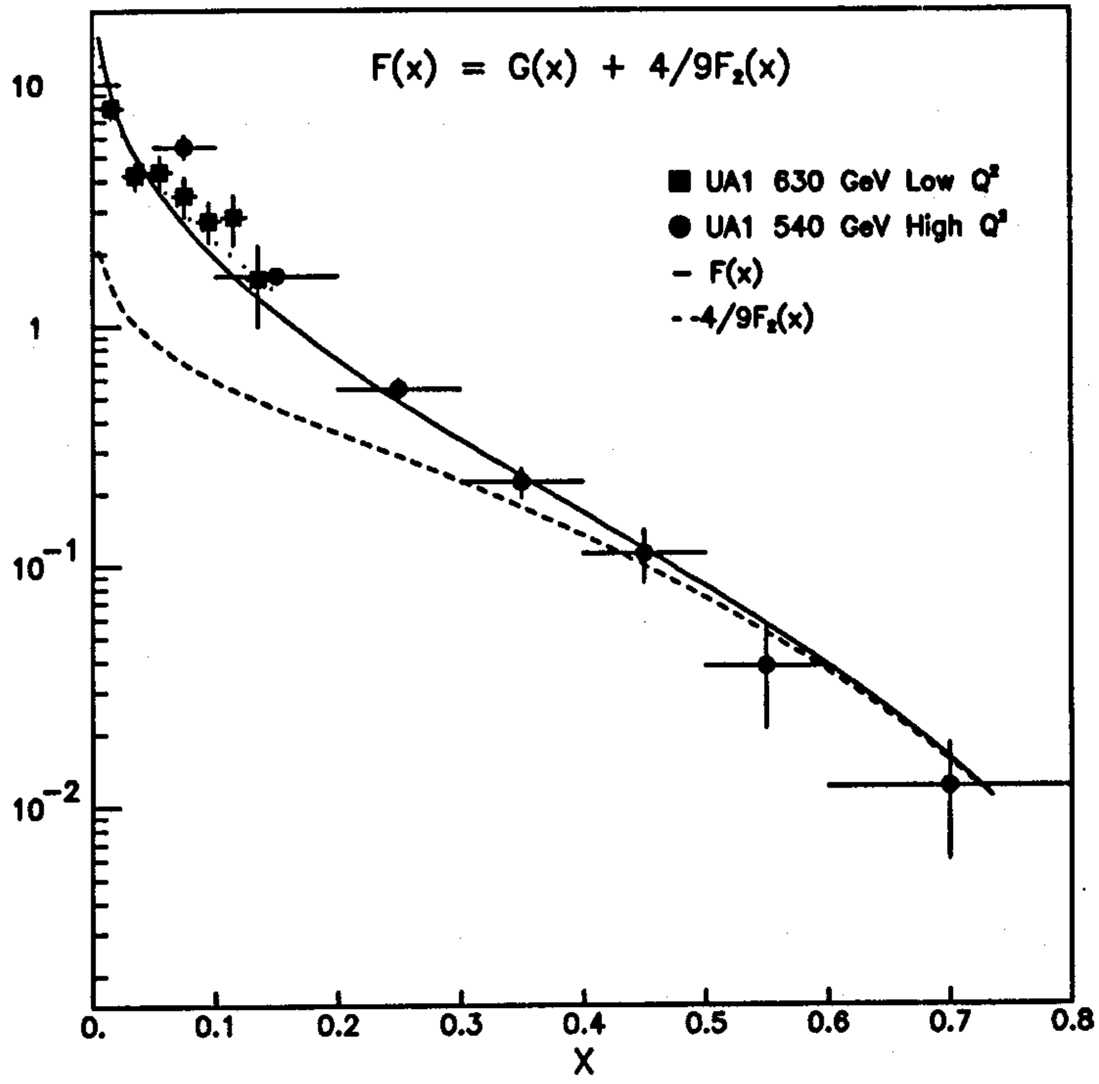
$F(x) = G(x) + 4/9F_2(x)$
■ UA1 630 GeV Low Q^2
● UA1 540 GeV High Q^2
– F(x)
- -4/9$F_2(x)$
10
1
10^{-1}
10^{-2}
0.
0.1
0.2
0.3
0.4
0.5
0.6
0.7
0.8
X

Fig. 5.8

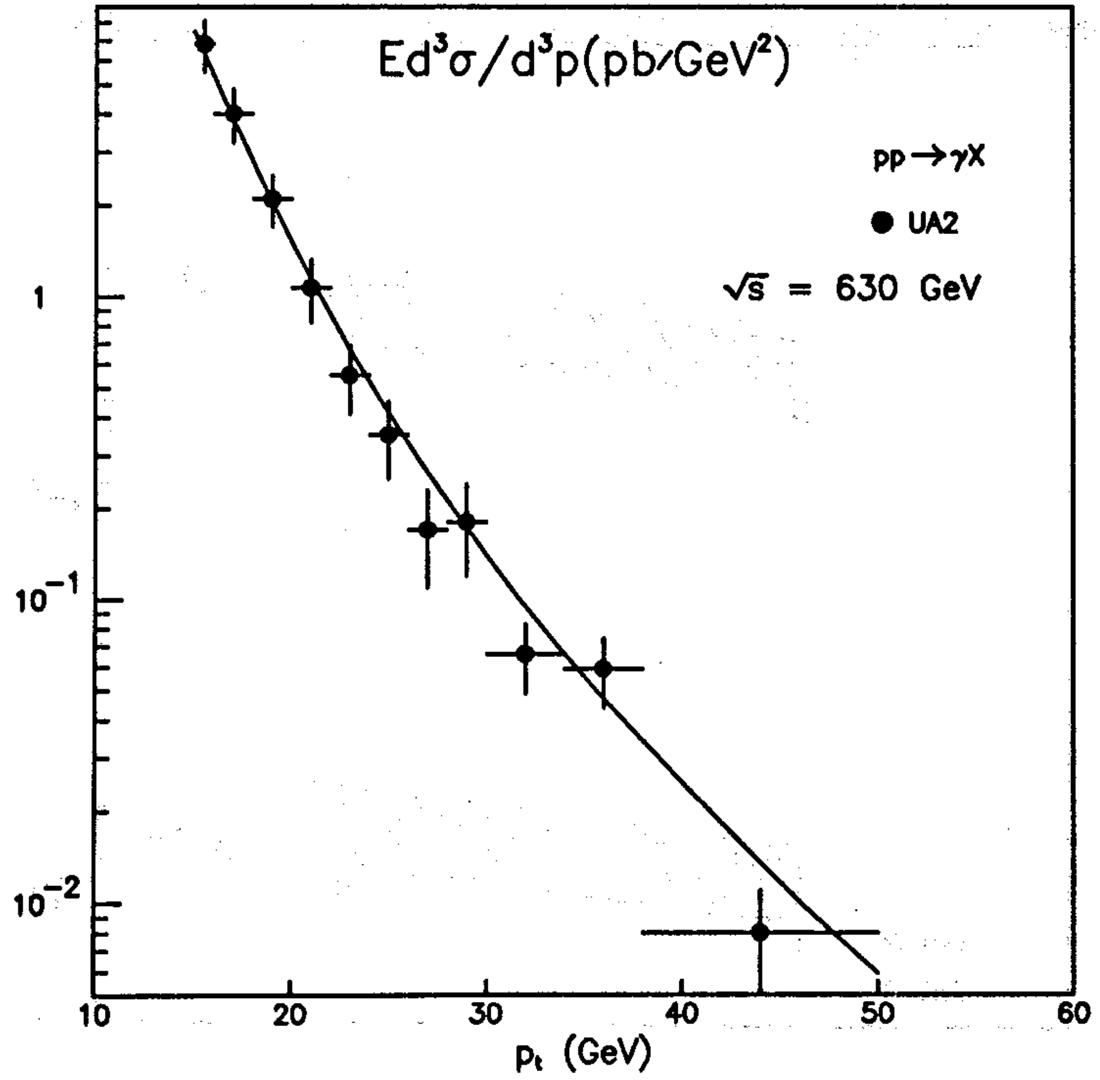
$Ed^3\sigma/d^3p(pb/GeV^2)$
$p\bar{p}\rightarrow\gamma X$
● UA2
$\sqrt{s}$ = 630 GeV
1
10^{-1}
10^{-2}
10
20
30
40
50
60
p_t (GeV)

Fig. 5.9

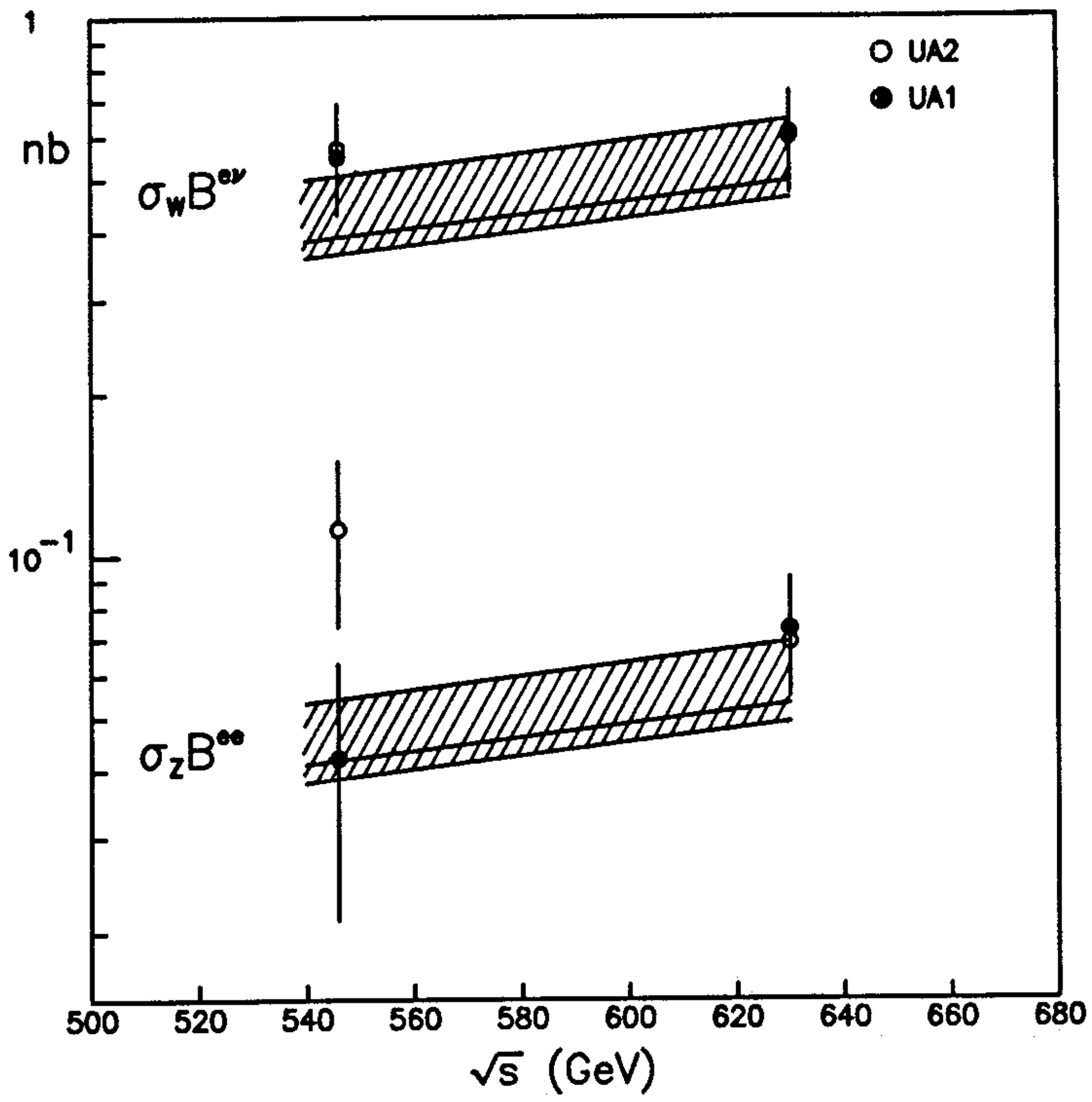
1
nb
10^-1
$\sigma_W B^{e\nu}$
$\sigma_Z B^{ee}$
○ UA2
● UA1
500
520
540
560
580
600
620
640
660
680
√s (GeV)

Fig. 5.10

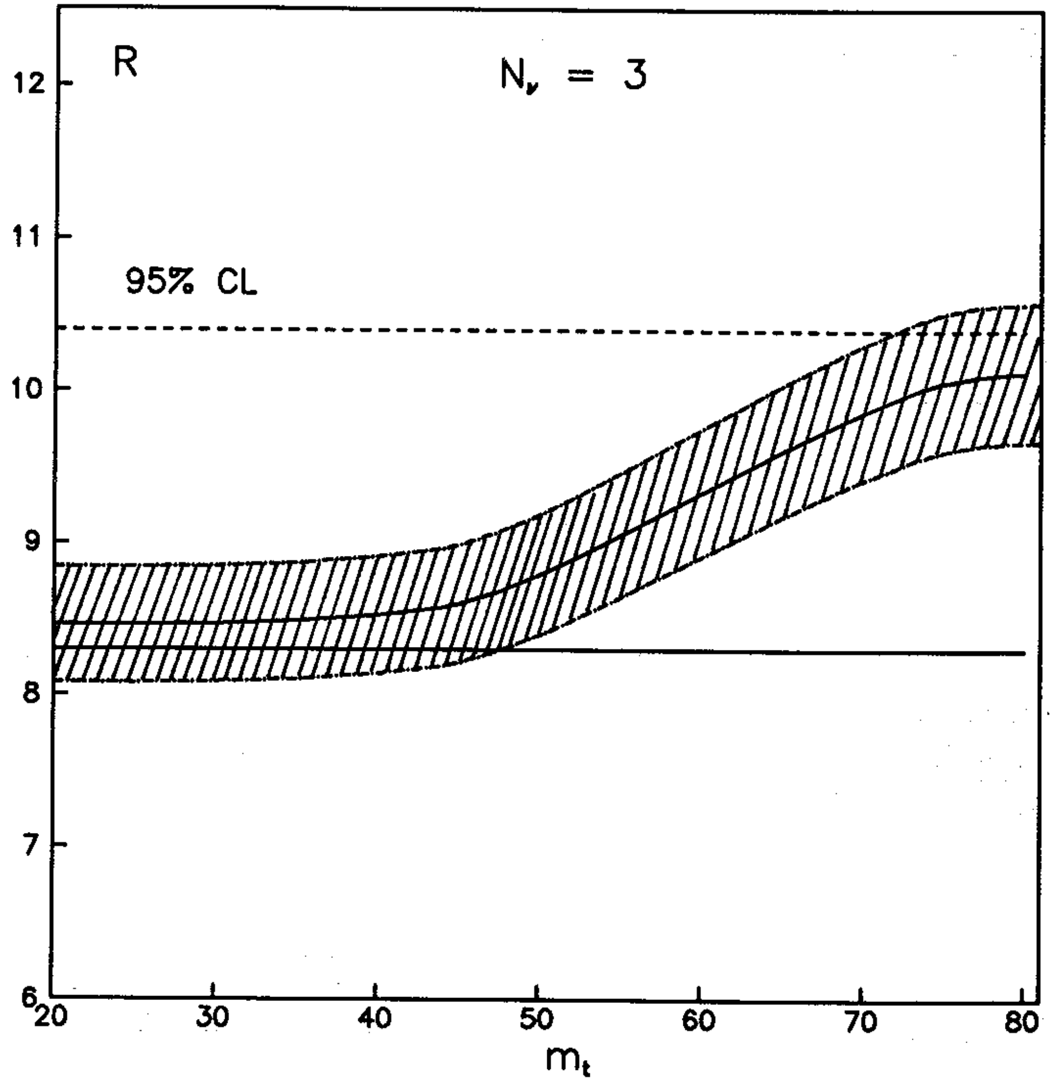

Fig. 5.11

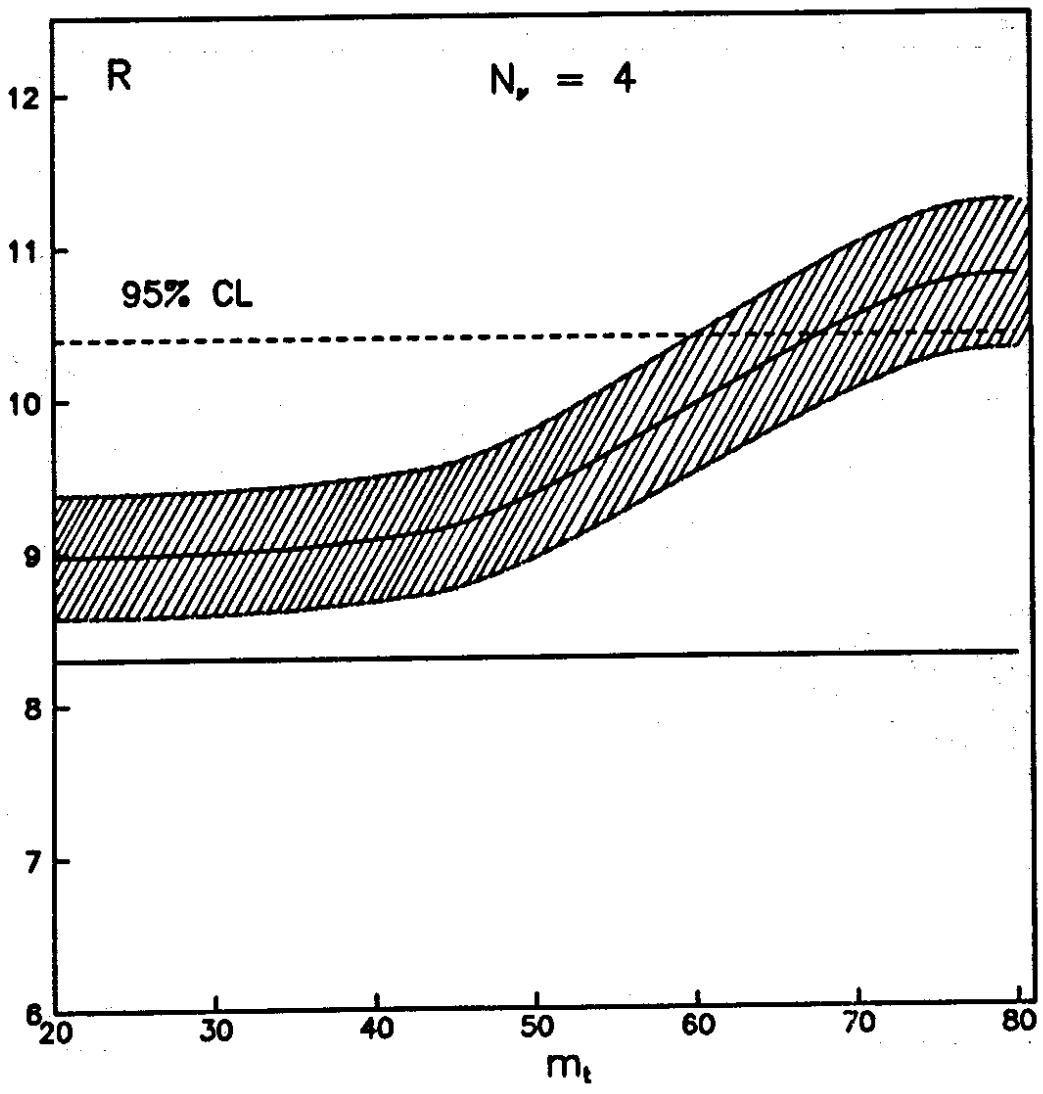

Fig. 5.12

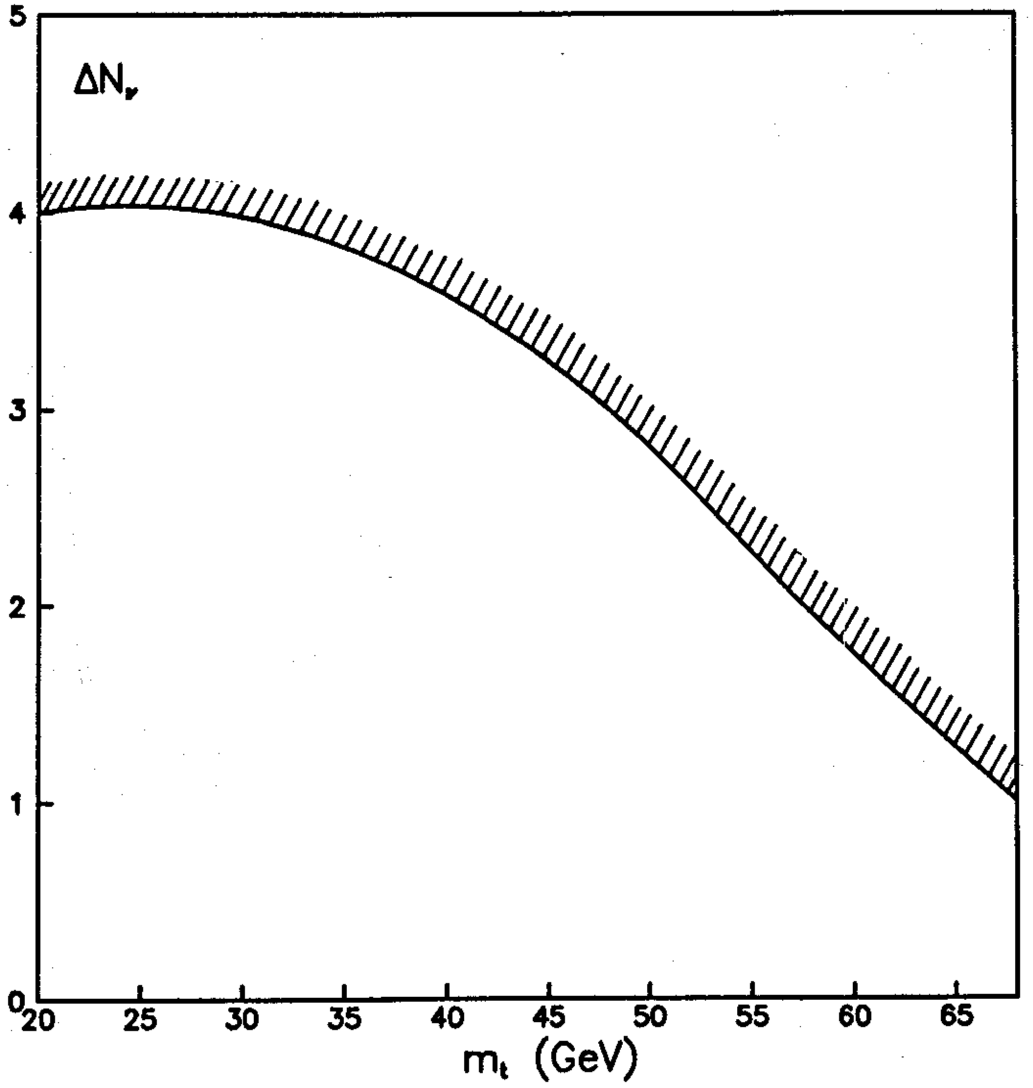

Fig. 5.13

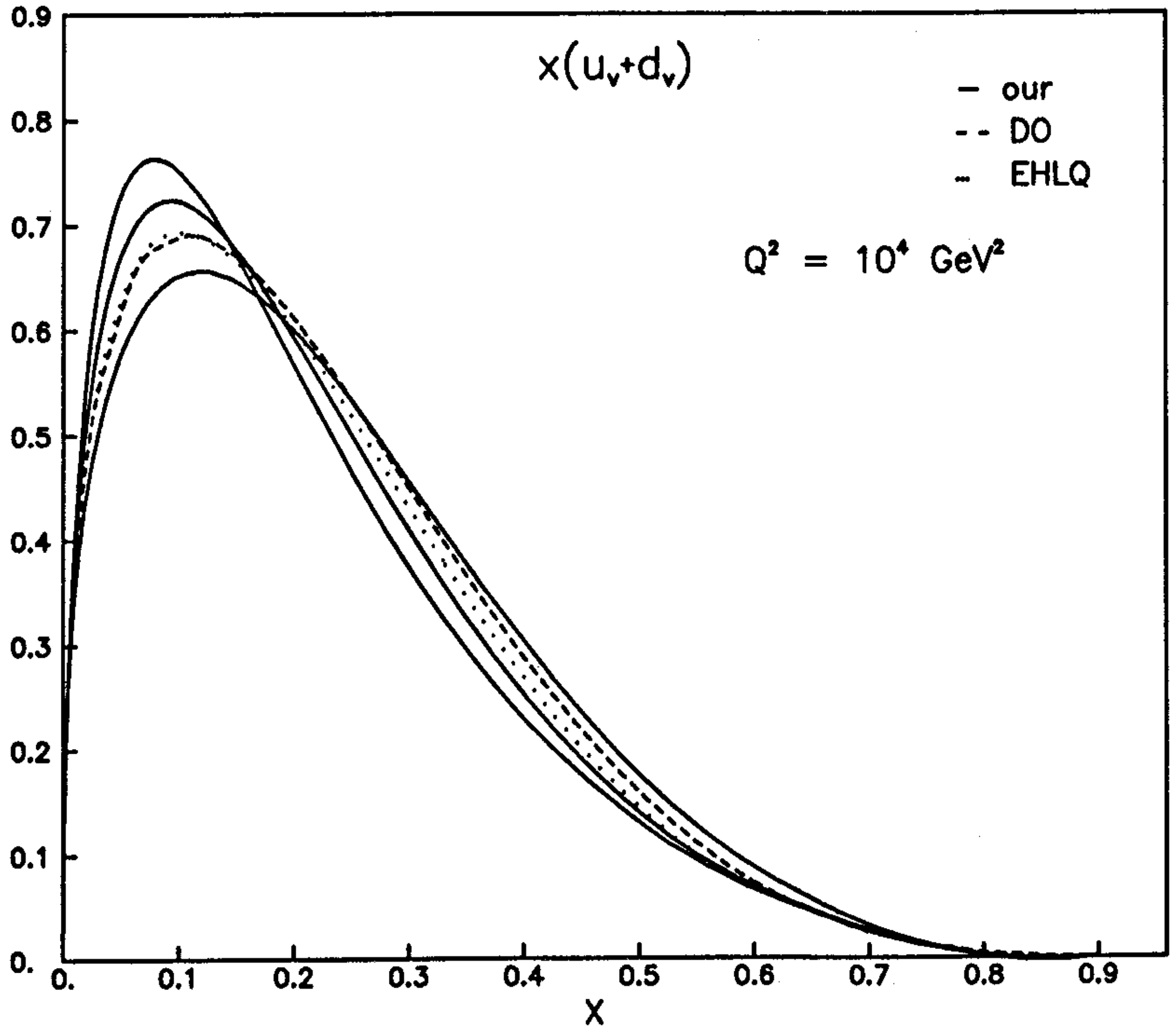
0.9
0.8
0.7
0.6
0.5
0.4
0.3
0.2
0.1
0.
x(u_v+d_v)
– our
-- DO
·· EHLQ
Q² = 10⁴ GeV²
0.
0.1
0.2
0.3
0.4
0.5
0.6
0.7
0.8
0.9
X

Fig. 6.1

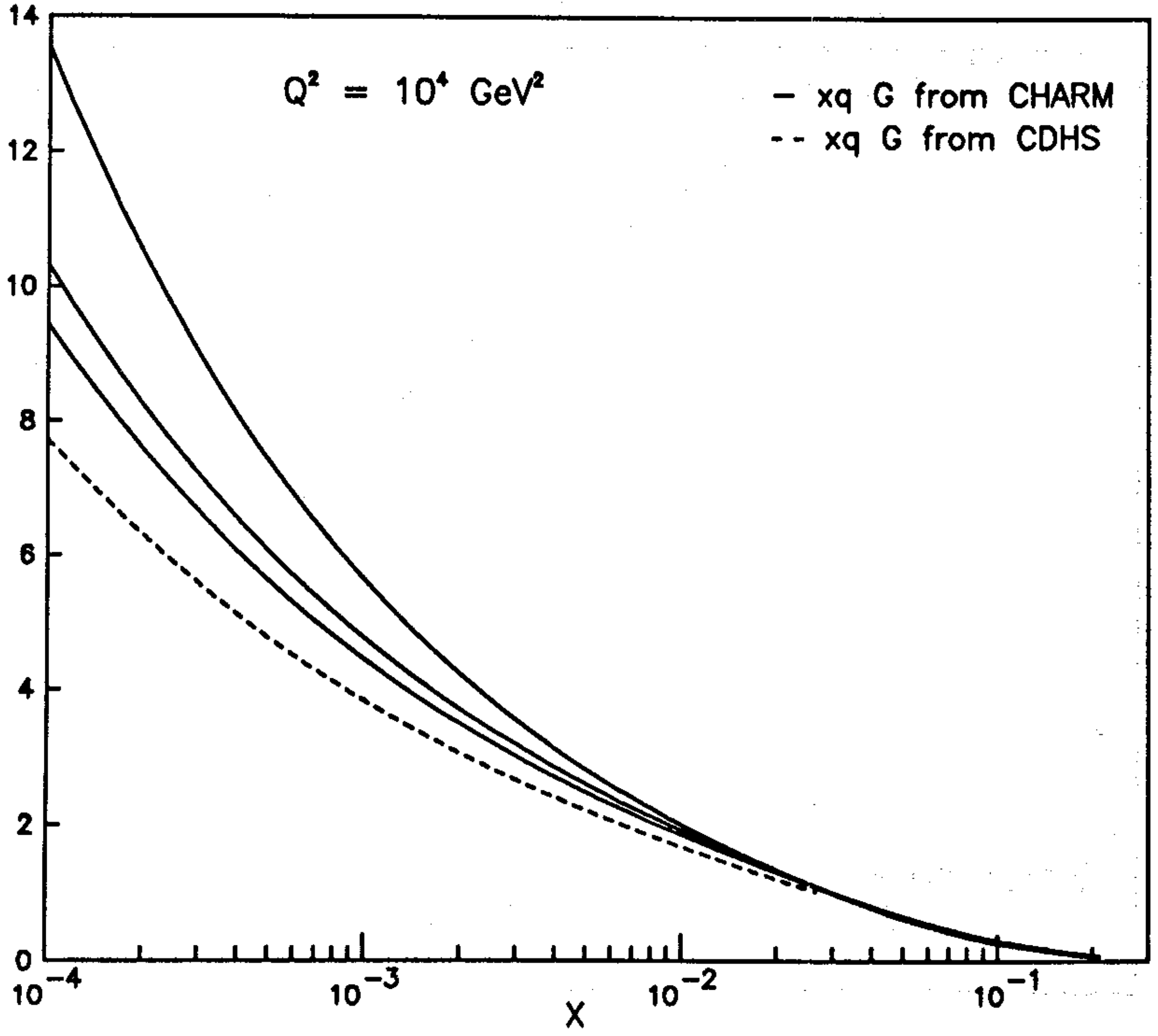
$Q^2 = 10^4$ GeV^2
— xq G from CHARM
- - xq G from CDHS
14
12
10
8
6
4
2
0
10^{-4}
10^{-3}
10^{-2}
10^{-1}
X

Fig. 6.2

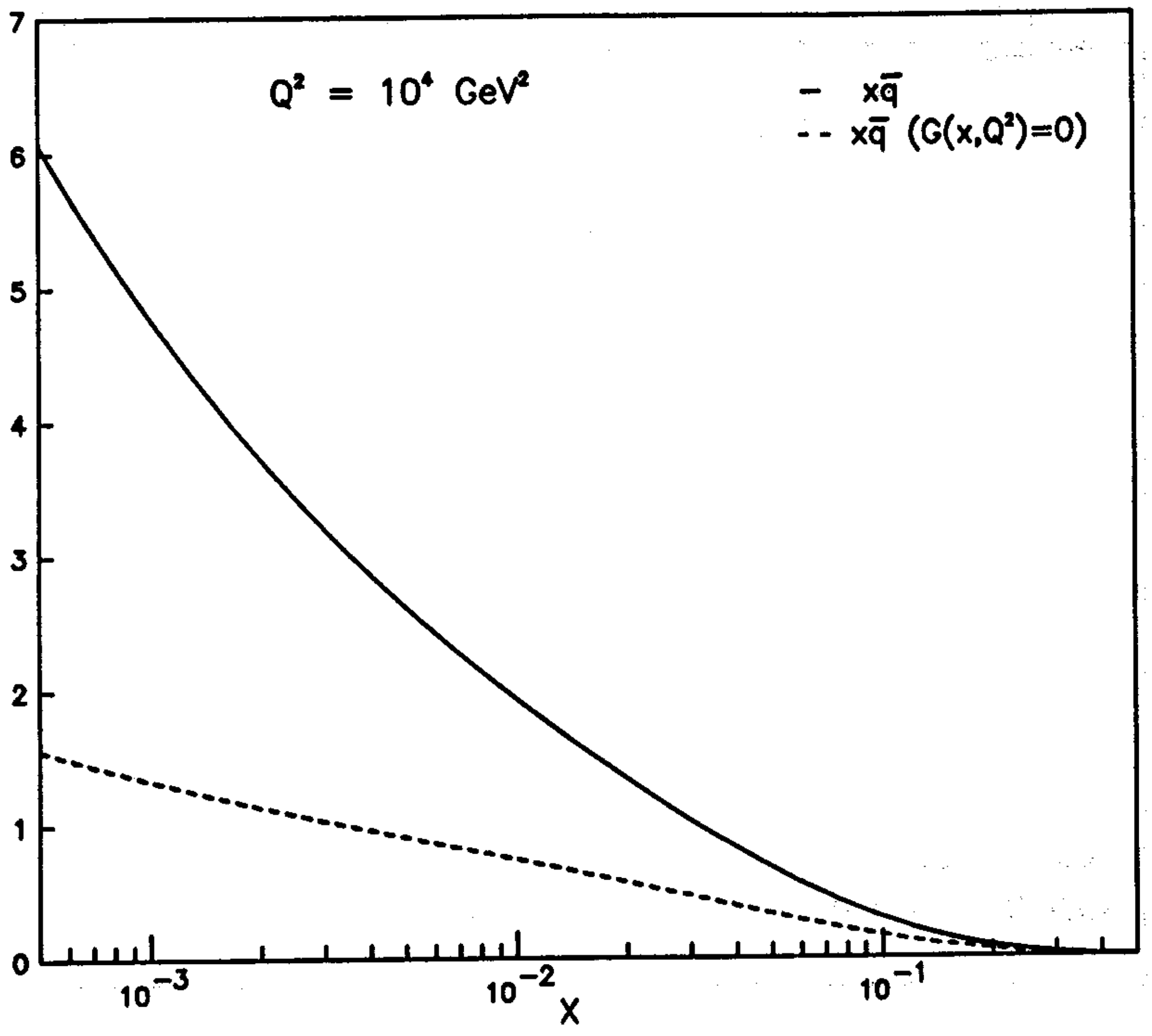

Fig. 6.3

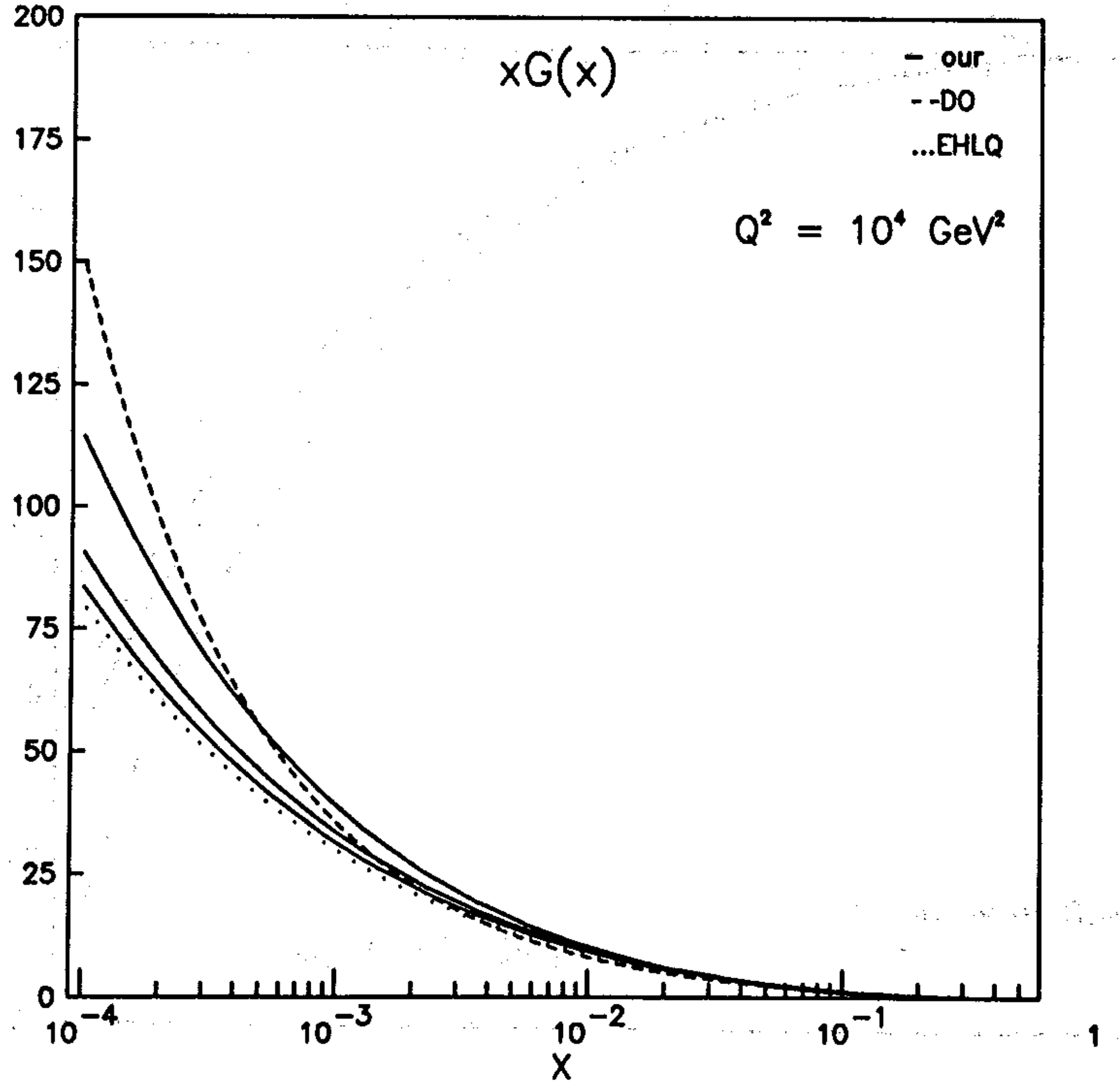
xG(x)
– our
- -DO
...EHLQ
$Q^2 = 10^4$ GeV^2
200
175
150
125
100
75
50
25
0
10^{-4}
10^{-3}
10^{-2}
10^{-1}
1
X

Fig. 6.4

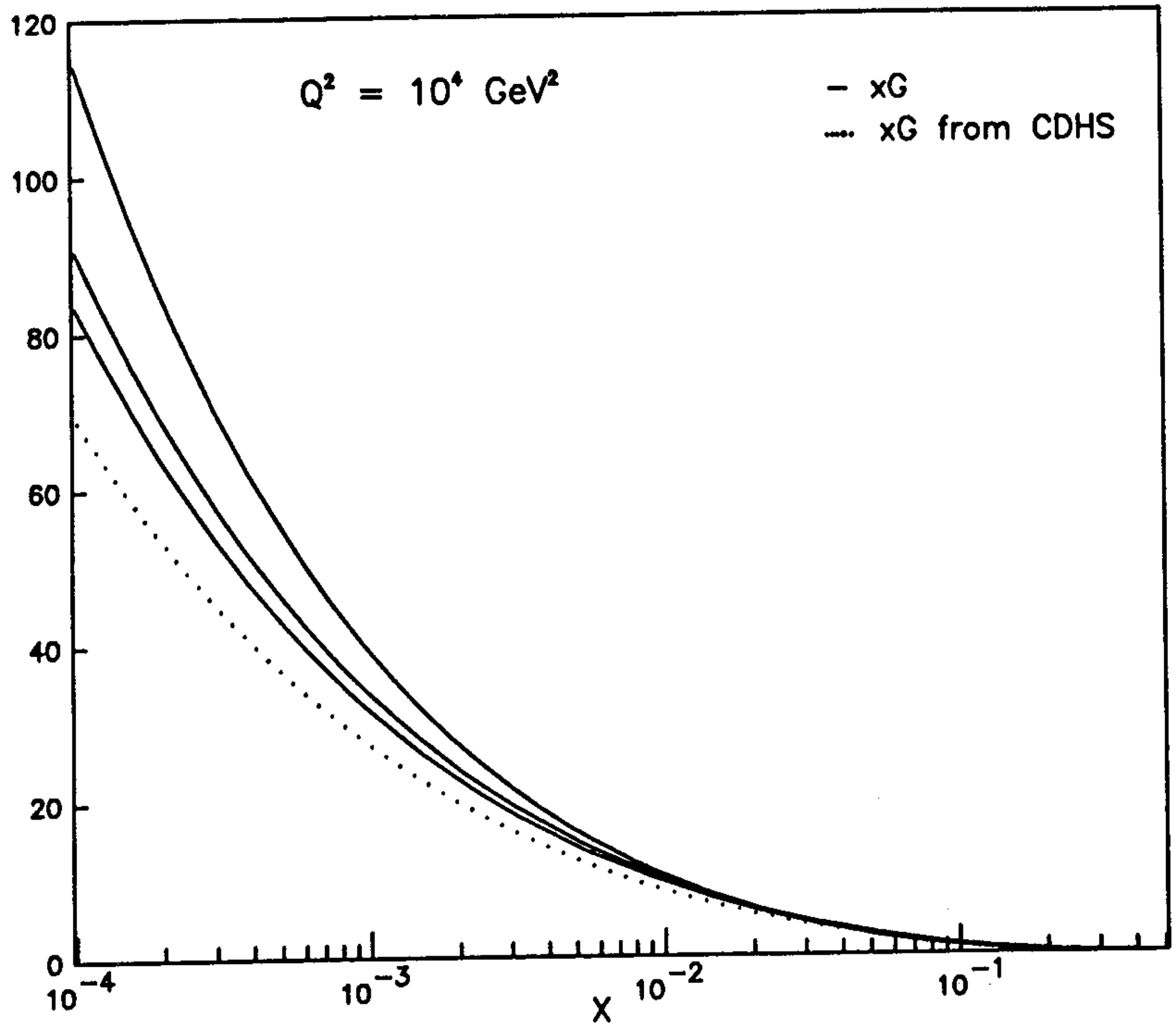

Fig. 6.5

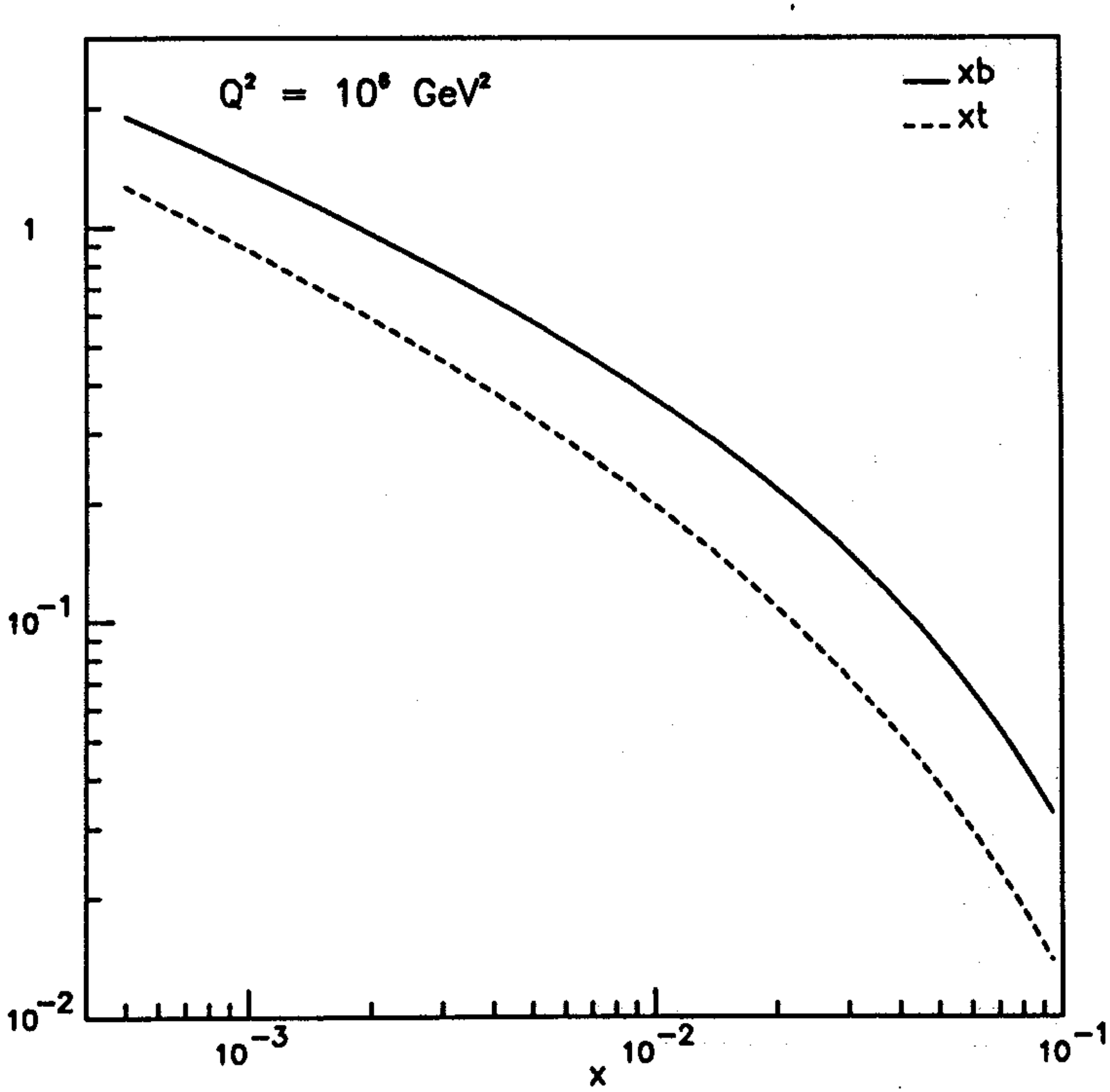

Fig. 6.6

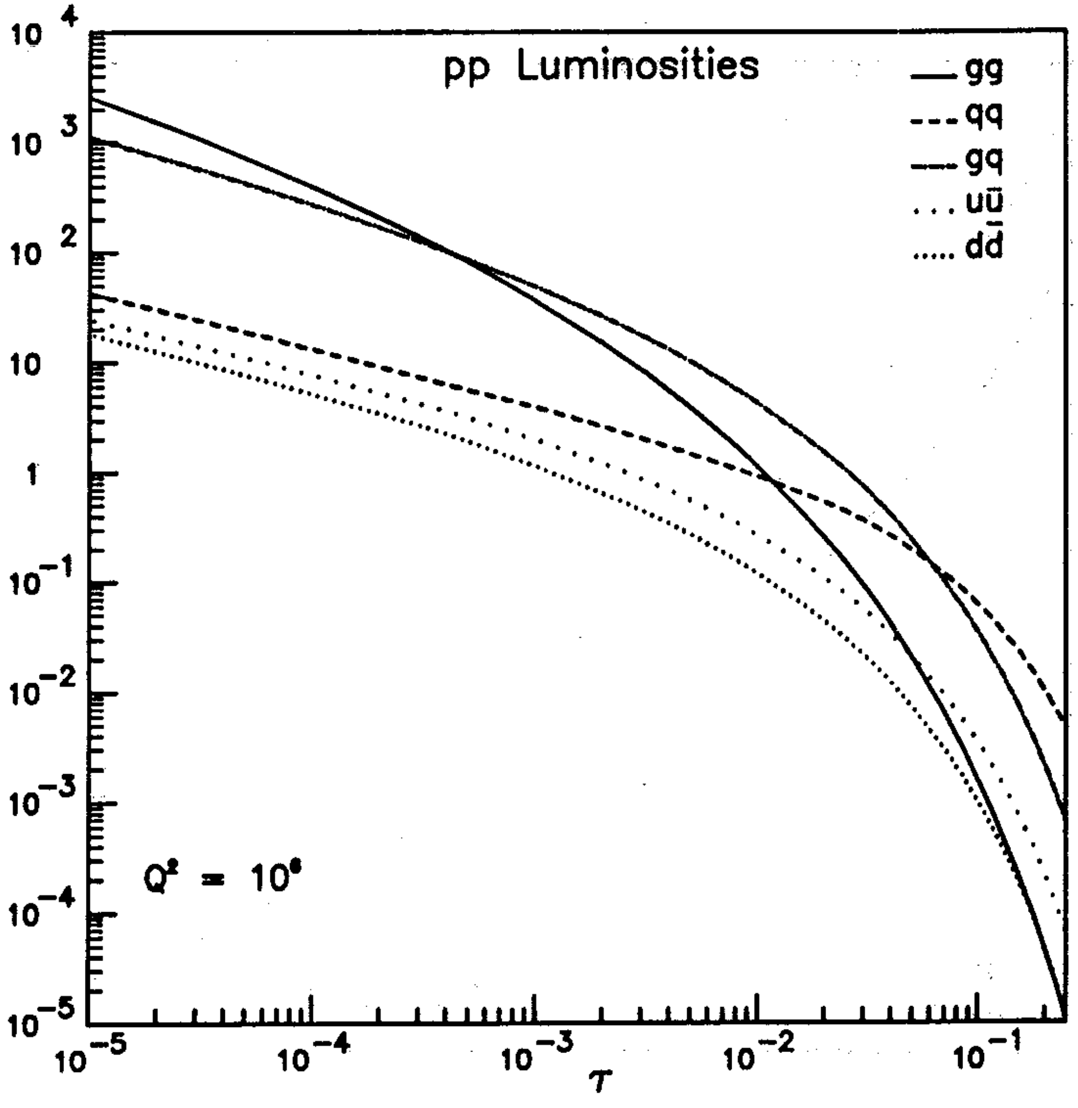
pp Luminosities
gg
qq
gq
uū
dd̄
$Q^2 = 10^6$
10 4
10 3
10 2
10
1
10−1
10−2
10−3
10−4
10−5
10−5
10−4
10−3
10−2
10−1
τ

Fig. 6.7

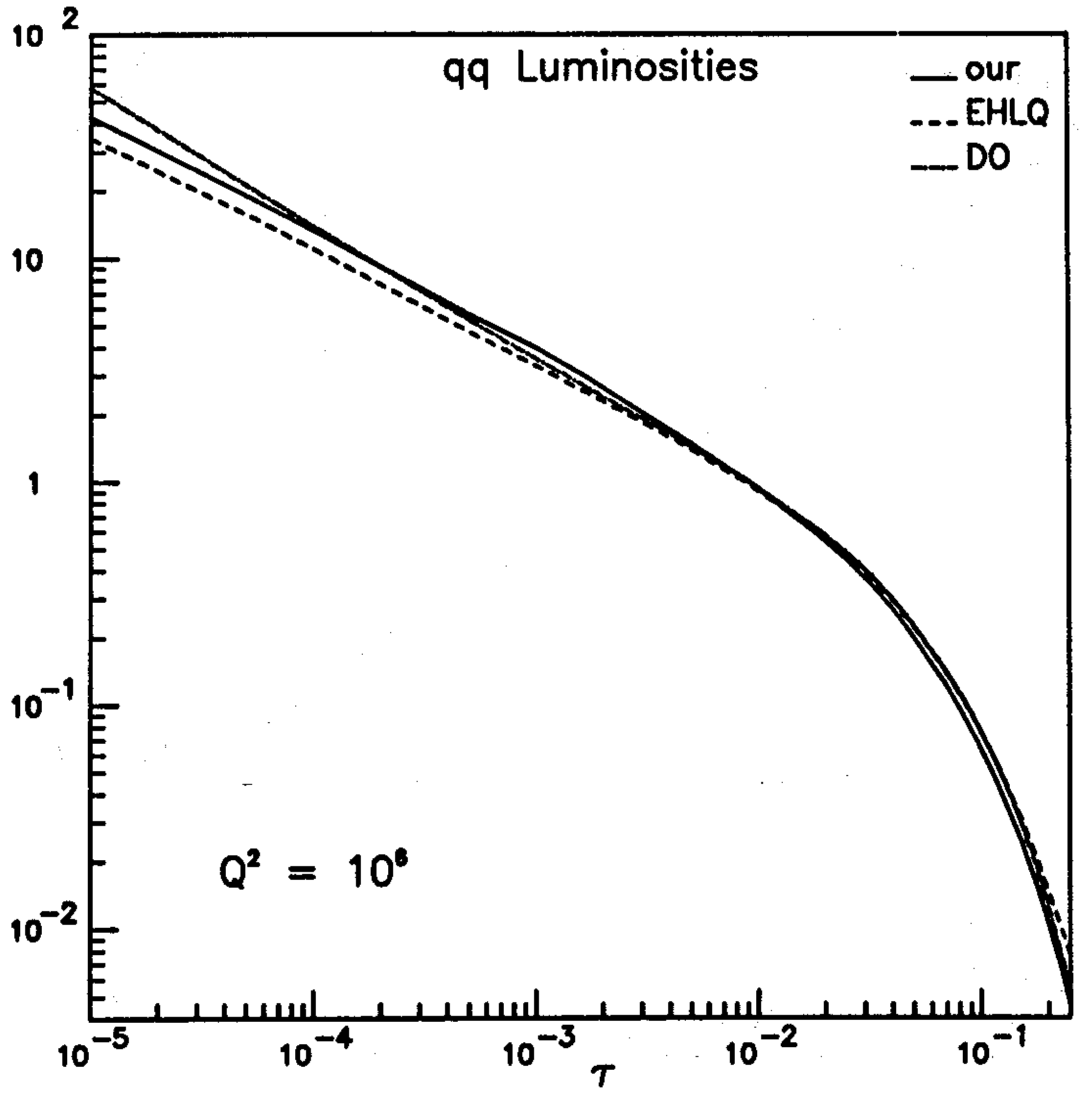
qq Luminosities
our
EHLQ
DO
$Q^2 = 10^6$
10^2
10
1
10^{-1}
10^{-2}
10^{-5}
10^{-4}
10^{-3}
10^{-2}
10^{-1}
τ

Fig. 6.8 a

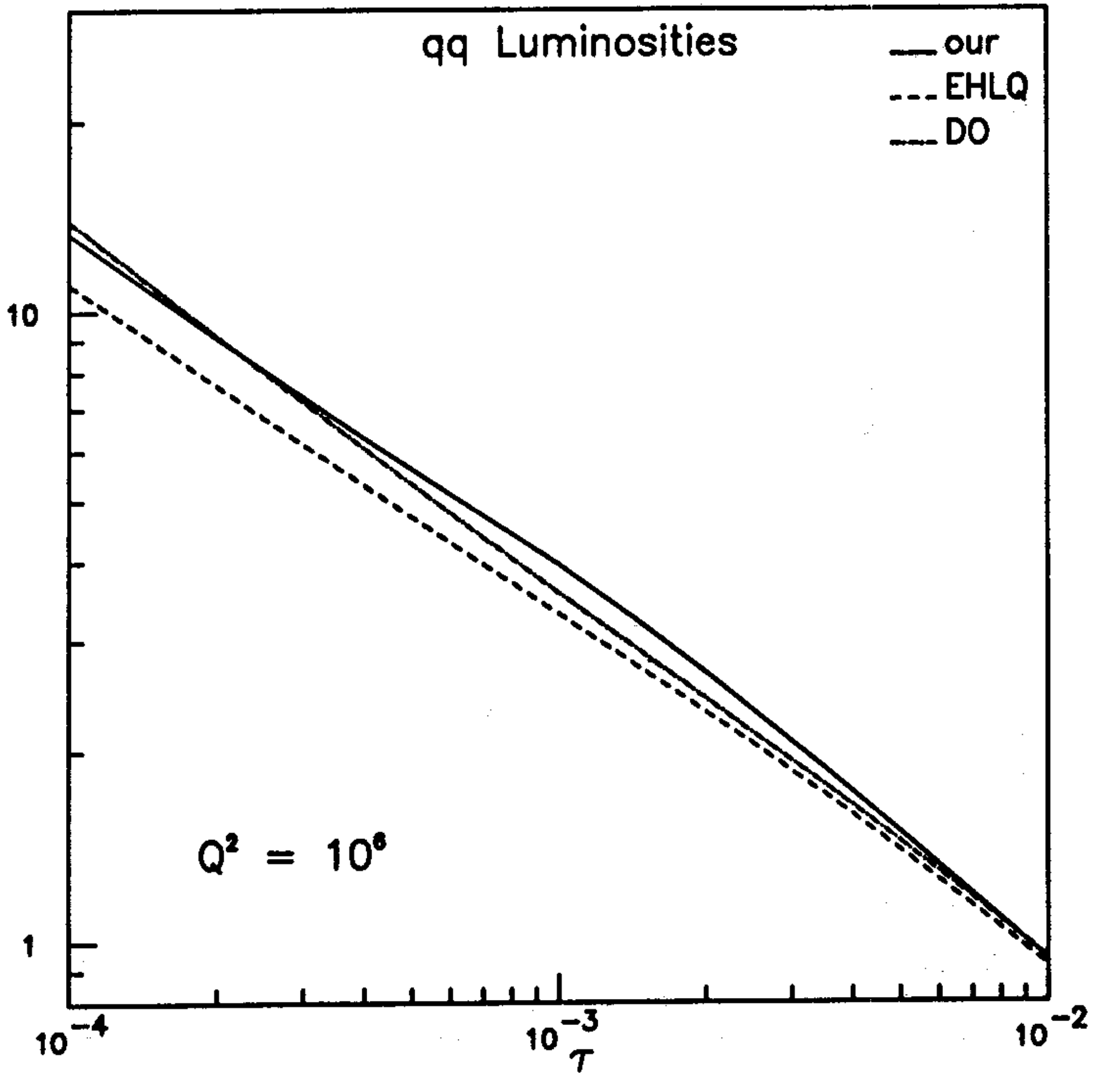

Fig. 6.8 b

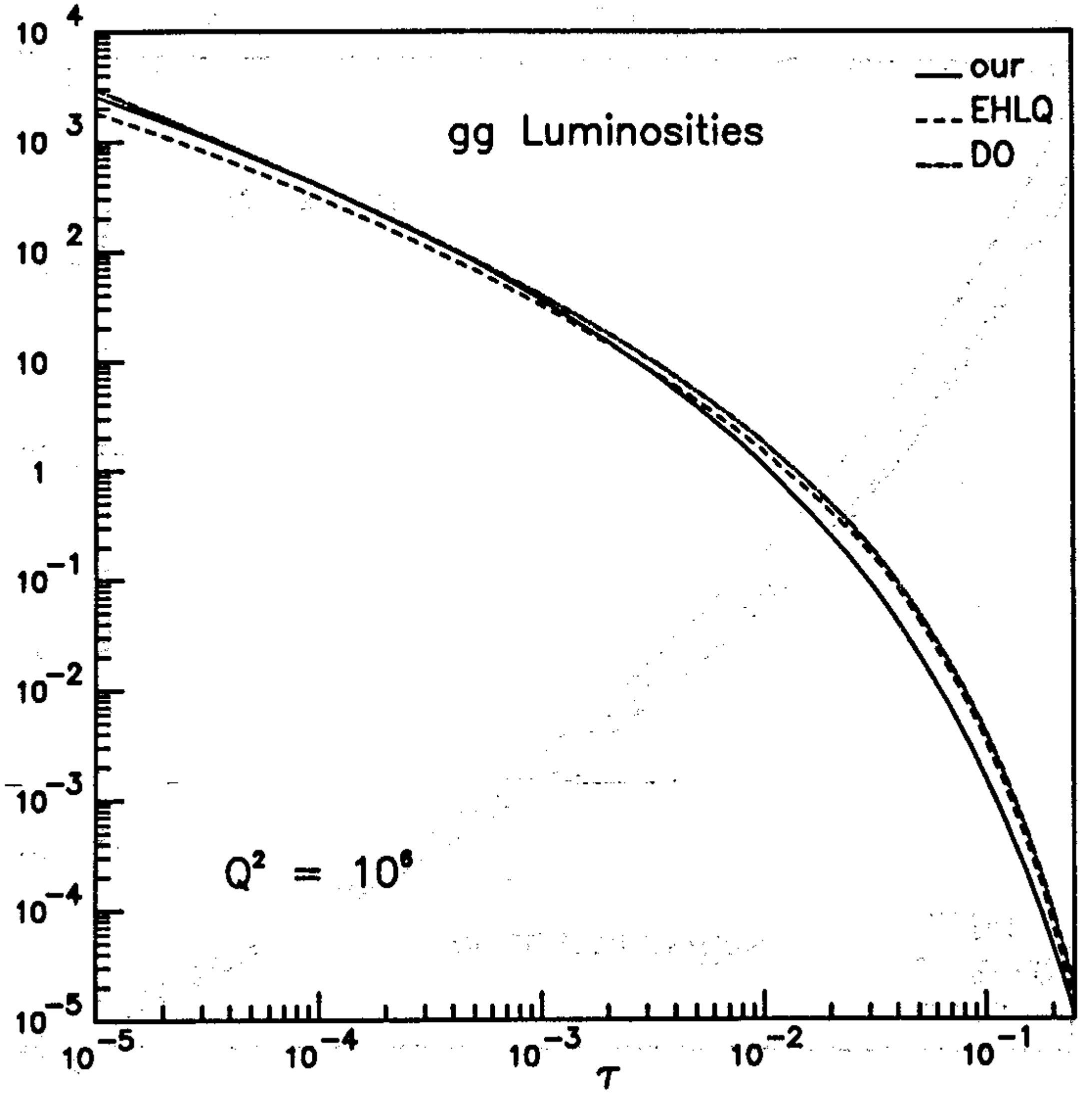
gg Luminosities
our
EHLQ
DO
$Q^2 = 10^6$
10^4
10^3
10^2
10
1
10^{-1}
10^{-2}
10^{-3}
10^{-4}
10^{-5}
10^{-5}
10^{-4}
10^{-3}
10^{-2}
10^{-1}
τ

Fig. 6.9 a

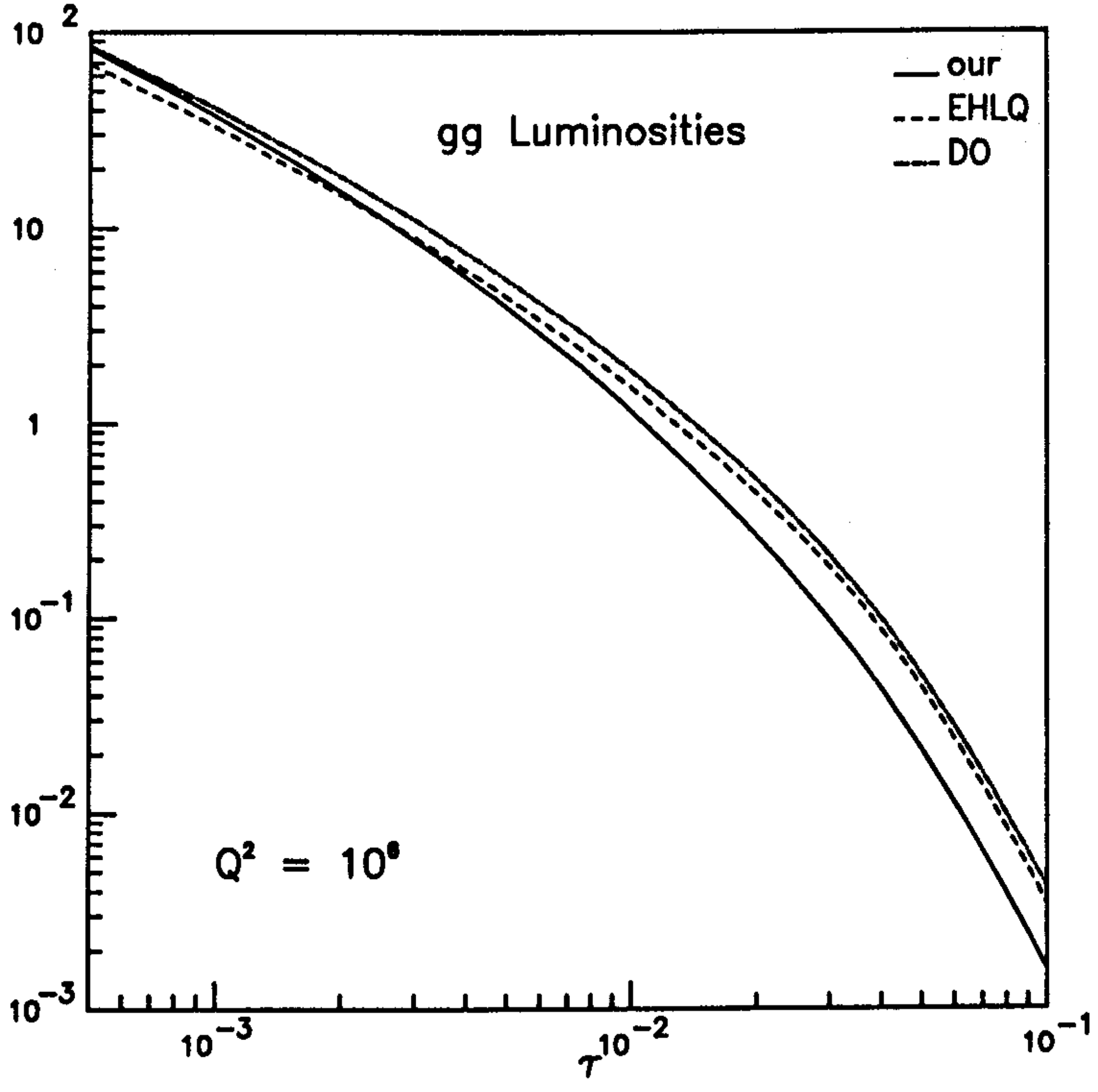
gg Luminosities
— our
--- EHLQ
—— DO
$Q^2 = 10^6$
10^2
10
1
10^{-1}
10^{-2}
10^{-3}
10^{-3}
10^{-2}
10^{-1}
τ

Fig. 6.9 b

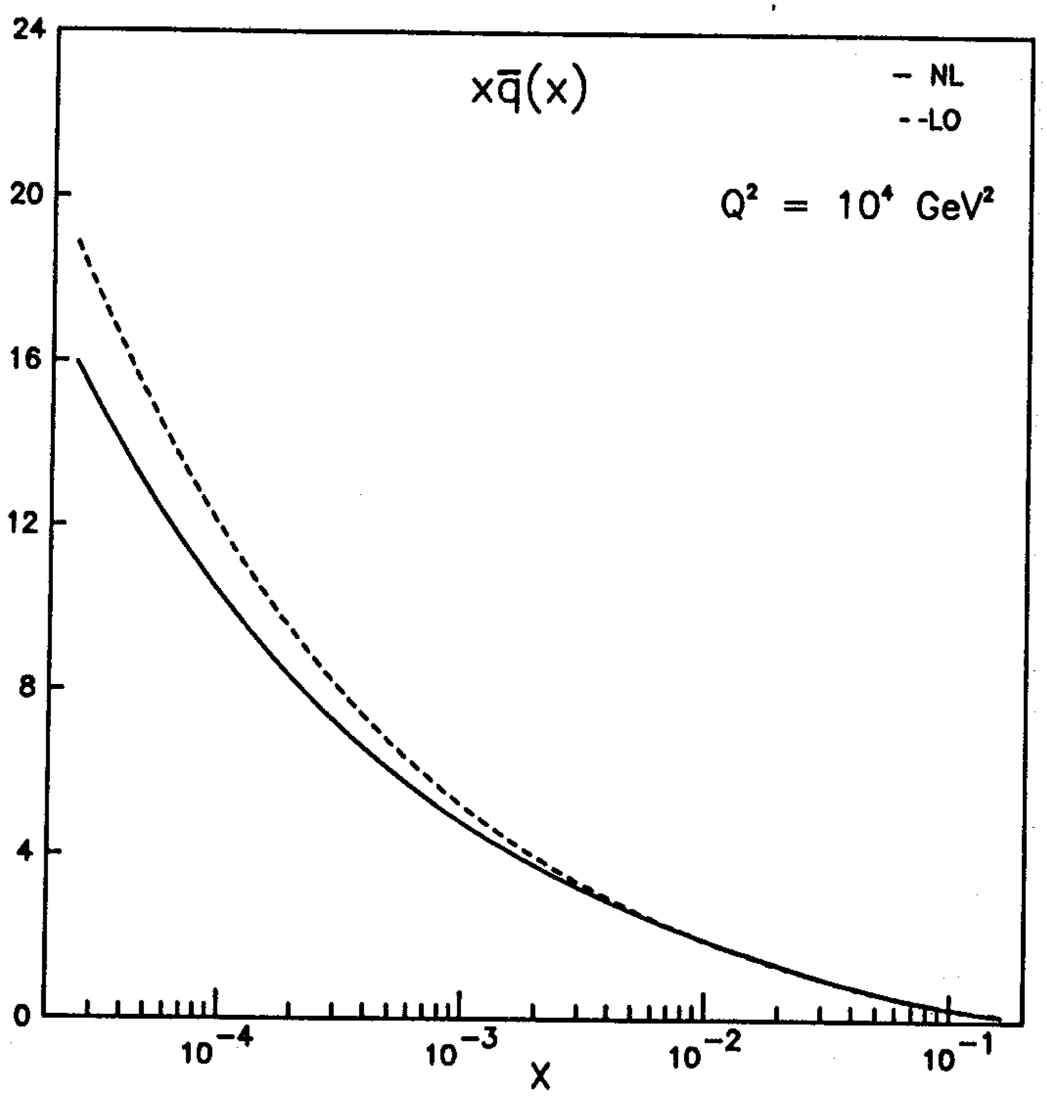

Fig. 6.10

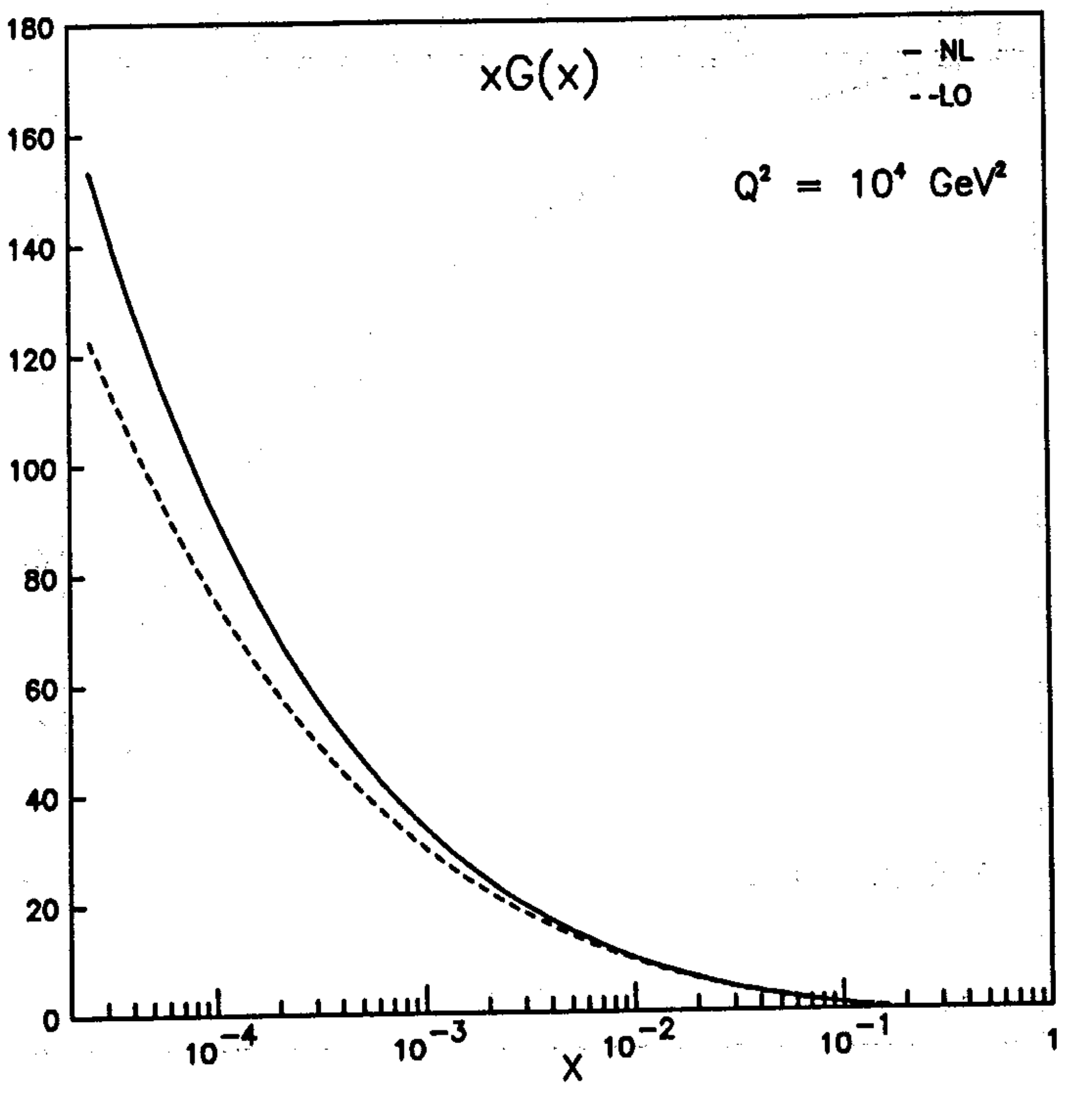
xG(x)
— NL
- -LO
$Q^2 = 10^4$ GeV^2
180
160
140
120
100
80
60
40
20
0
10^{-4}
10^{-3}
10^{-2}
10^{-1}
1
X

Fig. 6.11